AGU PUBLICATIONS

JGR

Journal of Geophysical Research: Solid Earth

RESEARCH ARTICLE
10.1002/2017JB014903

Special Section:
Rock Physics of the Upper Crust

Melt Welding and Its Role in Fault Reactivation and Localization of Fracture Damage in Seismically Active Faults

Kathryn S. Hayward[1] and Stephen F. Cox[1]

[1]Research School of Earth Sciences, Australian National University, Canberra, ACT, Australia

Key Points:
- Thin quenched layers of melt derived from frictional heating of asperity contacts weld fault surfaces, increasing cohesive strength
- Development of bypass fractures around welded zones results in transfer of material from one fault surface to the other, forming new asperities
- Widespread melt welding can cause fault lock-up and the failure of a new slip surface

Correspondence to:
K. S. Hayward,
kathryn.hayward@anu.edu.au

Citation:
Hayward, K. S., & Cox, S. F. (2017). Melt welding and its role in fault reactivation and localization of fracture damage in seismically active faults. *Journal of Geophysical Research: Solid Earth*, *122*, 9689–9713. https://doi.org/10.1002/2017JB014903

Received 22 AUG 2017
Accepted 8 NOV 2017
Accepted article online 11 NOV 2017
Published online 4 DEC 2017

Abstract Low displacement fracture damage plays an important role in influencing the behavior and mechanical evolution of faults. Fracture damage zones influence slip behavior through changing near-field stress orientations, altering fluid pathways and modifying fault structure. Here we use small displacement triaxial experiments to explore the development of fault zone damage, frictional lock-up, and the generation of new faults using samples with preground faults, oriented in 5° increments between 25° and 65° relative to the shortening direction. With increasing reactivation angle, faults support higher peak normal stresses (104–845 MPa) and behavior transitions from stable sliding to stick slip. Frictional melting occurs on surfaces where stick slip is initiated, forming micron-thick layers that locally weld asperity contacts. The extent of melt welding is correlated with normal stress and melt-welded zones increase fault cohesion. Distribution of fracture damage adjacent to the fault is spatially correlated with melt-welded zones and the corresponding concentrations of stress and elastic strain. In a process referred to as "adhesive wear," fractures bypassing welded zones transfer melt-adhered material from one side of the fault to the other, forming new geometric asperities. On faults with high reactivation angles (55°–60°) the increase in cohesive strength resulting from melt-welded contacts drives fault lock-up after an initial slip event; subsequent slip localizes on new, favorably oriented faults. Given their size, melt-welded zones are likely to be short-lived in nature but may play a significant and previously unrecognized role in the development of fault-related damage.

1. Introduction

Many faults remain active despite being unfavorably oriented for reactivation relative to the prevailing regional stress field (e.g., Fournier, 1996; Sibson, 1989, 1990, 2007). This suggests that faults are comparatively weak structures with reactivation occurring when large disparities exist between the cohesive strength and frictional properties of the fault zone and those of the surrounding rock mass. Sibson (1985, 1990) introduced terminology to describe faults depending on their orientation relative to the prevailing stress field. The terms "optimally oriented," "misoriented," and "severely misoriented" were coined to define faults in terms of the ratio of the effective principal stresses required to induce sliding. This definition requires knowledge of stress conditions and frictional properties of the fault, so for more general discussion where such parameters may not be known, faults are described in terms of being "favorably" or "unfavorably" oriented. Favorably oriented faults are close (±10°) to an ideal failure angle assuming frictional values consistent with Byerlee's law (Byerlee, 1978), whereas unfavorably oriented faults represent more significant deviations in orientation relative to the maximum principal stress. Examples of unfavorably oriented faults include low-angle normal faults (Wernicke, 1995), steep reverse faults (Sibson, Robert, & Poulsen, 1988), or segments of the strike-slip San Andreas Fault (Mount & Suppe, 1987).

Critical failure conditions for unfavorably oriented faults are notionally achieved through the evolution of stress states and pore fluid pressures (Cox, 2010; Scholz, 2002; Sibson, 1990; Streit & Cox, 2001), although some reactivations are attributed to chemically or physically induced fault weakness (e.g., dissolution-precipitation creep (Collettini & Holdsworth, 2004), the presence of frictionally weak mineral phases (Holdsworth, 2004), or the structure of the fault zone fabric (Collettini et al., 2009)). Processes occurring during the interseismic period, such as time-dependent evolution of frictional properties and cohesive strengthening through fault healing or sealing, can have significant implications for the reactivation of faults (Karner, Marone, & Evans, 1997; Tenthorey & Cox, 2006; Tenthorey, Cox, & Todd, 2003). Any increase in either the

frictional or cohesive strength of a fault results in the stress states necessary to reactivate a fault becoming increasingly similar to that required to generate intact rock failure (Cox, 2010; Streit & Cox, 2001). Where faults are unfavorably oriented for reactivation, even small increases in cohesive strength significantly reduce the range of conditions under which the fault can reactivate, leading to the failure of a new, favorably oriented fault (Sibson, 2012).

Field observations and recent experimental studies show near-instantaneous cohesive strength recovery occurring during seismic events where frictional melt is generated (Di Toro & Pennacchioni, 2005; Mitchell et al., 2016; Proctor & Lockner, 2016). As the melt cools, it solidifies, welding the fault surfaces and increasing the cohesive strength. Observation of some natural faults suggests that the formation of frictional melt, or pseudotachylyte, may hinder the reactivation of faults, with subsequent rupture events migrating to surrounding planes of weakness (Di Toro & Pennacchioni, 2005; Mitchell et al., 2016; Spray, 1995). Significantly, recent experiments undertaken at stress conditions equivalent to those in the midcrust to lower crust (normal stress 93–287 MPa) have shown that frictional melting occurs in dry conditions over slip distances of less than 100 μm at slip velocities greater than ~10 cm s^{-1}. This raises the possibility that frictional melting occurs, at least to some extent, during most, if not all seismic ruptures (Hayward et al., 2016). Melt welding might therefore be of widespread significance for the mechanics of fault rupture.

Despite the experimental work that has been undertaken, important unanswered questions remain: how do the thin layers of frictional melt at asperity contacts affect the strength and microstructural development of a fault during continued deformation? Are processes similar across a range of scales from small-scale asperity welding on experimental faults to large-scale melt welding of natural fault interfaces? Does the presence of thin glass layers affect the development of fracture damage zones? Can the cohesive strengthening resulting from melt welding be large enough to prevent the reactivation of unfavorably oriented faults? In this study we attempt to address these questions using experiments on preground fault surfaces ranging in orientation from favorable to unfavorable for reactivation. This configuration allows exploration of a wide range of normal stresses and the role that far-field stress orientations play in the development of fault microstructures.

2. Experimental and Analytical Methods

2.1. Experimental Methodology

The experimental material used during this study was Fontainebleau sandstone. It is an approximately equigranular, almost pure quartz (>99%) sandstone with grain size of 150–200 μm and a porosity between 6 and 8%. The detrital grains are well cemented by syntaxial quartz overgrowths, resulting in a subhedral to euhedral grain shape. Samples were prepared by coring 10 mm diameter cylinders, with an overall specimen length of 21 mm. Surfaces were ground using a 30 μm water-cooled lapping wheel so that the sample ends were perpendicular to the cylinder axis and any preground fault surface was flat and accurately oriented relative to the shortening direction. All samples were kept in a drying oven at 70°C for a minimum of 96 h before use.

Deformation experiments were performed using two different experimental configurations. The strength and mechanical properties of the sandstone were estimated during the first suite of experiments that involved brittle failure of intact rock cylinders over a range of confining pressures (P_c = 15–70 MPa) (Figure 1a). Each of the second suite of experiments, here referred to as fault reactivation experiments, used two cylinders of sandstone ground to a specific angle between 25° and 65° relative to the axial shortening direction. The ground surfaces represent faults that vary in orientation from favorably to unfavorably oriented for reactivation (Figure 1b). Experiments were undertaken at confining pressures (P_c) of 50 and 100 MPa.

Surface roughness and microstructural characteristics of the preground surfaces were characterized using both a Leica DCM8 optical surface measurement system and scanning electron microscopy (SEM). At the larger scale, surface topography is controlled by the pore structure of the sandstone with pores up to 100 μm in depth. The slip surfaces show little evidence of grain plucking resulting from the surface preparation process. At the grain scale, roughness is determined to be <10 μm (Figure 1c). Wear tracks, surface fracturing, and

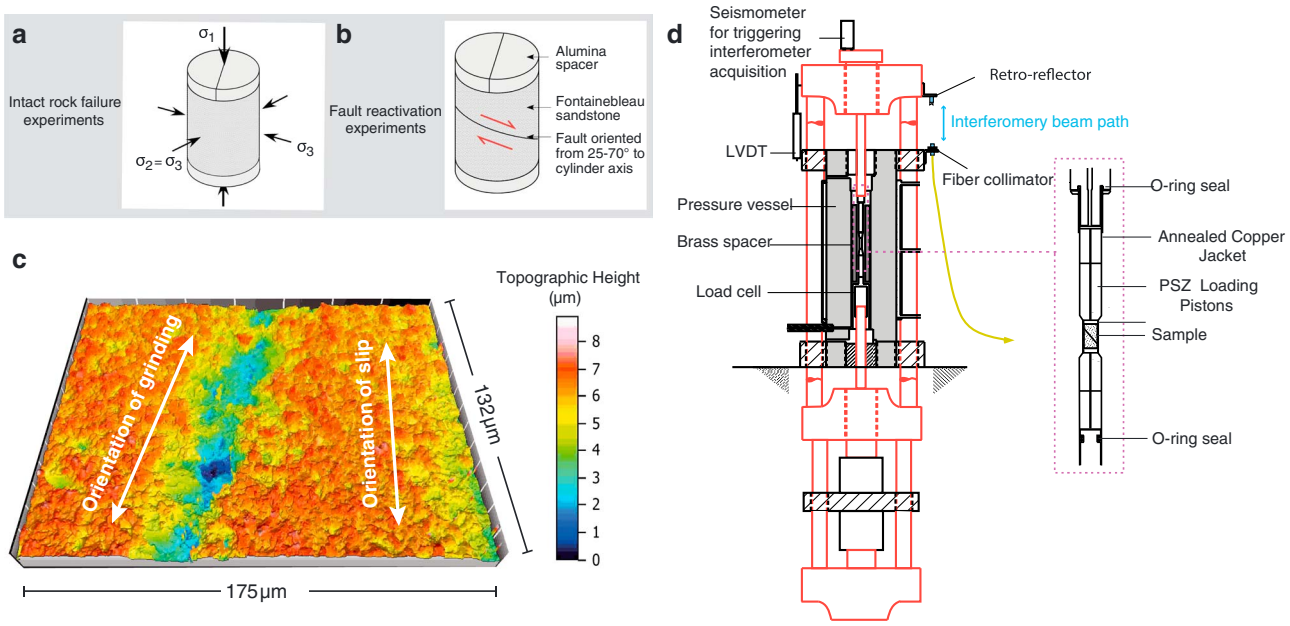

Figure 1. Sample configuration, fault surface roughness, and apparatus. (a) Sample configuration for intact rock failure experiments. (b) Sample configuration for the fault reactivation experiments. Fault orientation is changed in 5° increments, with reactivation angles of 25°–65° relative to the axial shortening direction. (c) Representative image taken using a surface-profiling microscope showing surface topography of a ground quartz grain on the fault surface. Subtle lineations (depth less than 10 μm) are present on fault surfaces. These striations result from the position that the sample is held in the sample holder during surface grinding and are inclined at 10°–15° to the slip direction in experiments. (d) Diagram showing the main system components of the gas-medium deformation apparatus and the sample assembly. The fiber collimator and retro-reflector create the beam path of the laser interferometer used to record displacement during fast slip events. The seismometer shown at the top of the apparatus is used to trigger acquisition of the interferometry data.

spalling resulting from the grinding process are evident, although minimal debris remains on the surface after ultrasonic cleaning.

All experiments were undertaken at room temperature and in nominally dry conditions using a Paterson gas-medium, rock deformation apparatus (Figure 1d) (Paterson, 1970). Samples are loaded until failure or reactivation at constant axial displacement rate of 3.6 μm s^{-1}. Mechanical data were recorded using a Labview digital data acquisition system. Noise reduction was achieved through synchronizing the acquisition clock to the electricity mains supply and sampling at a frequency of 100 Hz. Samples are averaged and recorded at a rate of 1 sample per second. No electronic filters were used.

2.1.1. Recording Displacement at High Frequencies During Fast Slip Events

To show the potential for fault surfaces to generate temperatures sufficient to melt Fontainebleau sandstone at room temperature, an additional experiment was undertaken using a custom-designed optical fiber-based interferometer to record high-speed displacement data. The interferometry system is described in detail in Hayward et al. (2016) and supporting information, and uses a 1550 nm fiber-based Mach-Zehnder optical heterodyne system coupled with a digital phase lock loop to provide noncontinuous, triggered acquisition at a recording rate of 1 million samples per second. The beam path is located on the exterior of apparatus, with optical collimator mounted at the top of the pressure vessel (Figure 1c). The laser beam is reflected off a mirror attached to the apparatus yoke providing a path that varies during deformation. Displacement measured using the interferometer is calibrated against the displacement data recorded in an equivalent location by the linear voltage differential transducer and has been corrected for elastic distortion of the apparatus.

2.1.2. Apparatus Stiffness

The apparatus used to perform the current suite of experiments is considered a "soft" apparatus, as it accumulates significant elastic strain during loading; stored elastic strain is imparted into the specimen during failure, resulting in higher displacements and stress drops than could be achieved using a more rigid apparatus. All displacement measurements reported for these experiments have been corrected for the elastic contribution of the apparatus. Elastic response of the apparatus has been calculated using a series of experiments

undertaken on a test sample with known material properties and is linearly proportional to the applied force. The elastic response is approximately 0.0149 mm/kN axial load.

2.1.3. Correction for Jacket Strength

The sample is isolated from the confining medium using a thin-walled, annealed copper sleeve and jacket (wall thickness 0.25 mm) (Figure 1d). A correction for the strength contribution of the jacketing material was applied to the experimental data based on a series of calibration experiments performed on a low shear strength test assembly. A 0.5 mm thick graphite foil was placed between two alumina forcing blocks ground at 30° to the shortening direction. Calibration experiments were undertaken over a range of confining pressures (P_c = 5–200 MPa) using both a double-jacketed assembly (comprising of an outer jacket and inner sleeve) and a single-jacketed assembly. The assembly strength at 0.5 mm displacement over the range of confining pressures was used to construct a failure envelope. The intercept between the envelope and the load axis has provided an estimate of the strength of the assembly at zero confining pressure, where it is assumed that the dominant strength of the assembly arises from the pressure-insensitive jacket contribution. Each of the corresponding double- and single-jacketed strength estimates were subtracted to provide the strength of the metal sleeve. Total jacket strength is assumed to be proportional to the total cross-sectional area of the metal jacketing and at room temperature is estimated to be ~42 MPa at 0.5 mm displacement or ~4% of the maximum measured differential stress.

To apply the jacket strength correction to the experimental data, it is assumed that the yield point of the fault controls the yield of the jacket assembly. For simplicity, at the experimental yield point, the jacket and sleeve are assumed to simultaneously achieve both the calculated strength and a state of perfect plasticity. Prior to yield the load that the jackets support is assumed to increase linearly with displacement, and thus, the following two-stage approach to the jacket correction has been adopted.

Sample strength as a function of time ($\sigma_S(t)$) is given by

$$\sigma_s(t) = \frac{F_T - \left(\frac{t-t_0}{t_Y-t_0} \cdot F_{J,SI}\right)}{A_S}, t < t_y$$

$$\sigma_s(t) = \frac{F_T - F_{J,SI}}{A_S}, \quad \text{otherwise} \tag{1}$$

where F_T is the total force recorded by the load cell, t is time, t_0 is the time at which the experiment commenced, t_Y is the time at yield, and A_S is the cross-sectional area of the sample perpendicular to the direction in which the axial force is applied.

2.1.4. Correction for Change in Cross-Sectional Area

With continued slip on the fault interfaces, displacement results in a reduction in the contact area of the fault interface. A reduced contact area results in an increase in stress on the remaining interface; this effect is most significant on faults inclined at a high angle relative to the sample axis. A correction has been applied to the data by calculating the change in fault surface area as a function of shear displacement, assuming that displacement on the fault occurs only during the periods of nonelastic strain.

2.2. Microstructural Analysis Techniques

Following removal of the sample from the pressure vessel, the outer copper jacket was peeled off leaving the sample contained within the inner copper sleeve. To preserve any loose wear/damage products, the sample was impregnated with a heat-curing epoxy. Once cured the sample was cut along the long axis, parallel to slip direction of the fault. Half of the sample was then mounted in epoxy, polished and carbon coated for analysis using backscattered electron scanning electron microscopy (BSE-SEM). Microscopy was undertaken using a four quadrant solid-state backscattered detector (AsB), a working distance of between 6 and 10 mm, 5.0–10.0 kV accelerating voltage using high current, and a 60 μm aperture.

The slip surfaces of a number of representative samples were also examined. These samples were prepared by carefully peeling the copper sleeve from around the sample. The two halves of the fault were mounted on SEM stubs using Crystalbond polymer so that the surfaces were horizontal and parallel. The samples were coated in platinum and the fault surface textures were imaged using the in-lens secondary electron (SE) detector of the high-resolution Zeiss UltraPlus field emission scanning electron microscope (SEM).

Table 1
Failure of Intact Rock Samples

No.	Angle θ (deg)	Confining pressure (MPa)	Axial disp. rate ($\mu m.s^{-1}$)	Peak diff. stress (MPa)	Peak shear stress (MPa)	Peak normal stress (MPa)	Stress drop during slip event (MPa)	Shear disp. During slip event (mm)	Total exp. disp. (mm)
IRF006	16	15	3.63	588	165	61	406	0.694	1.28
IRF005	17	30	3.63	664	186	88	480	0.796	1.66
IRF003	26	50	1.78	838	330	211	545	1.044	2.560
IRF018	23	50	3.63	811	302	186	502	0.850	1.35
IRF001	24	52	1.78	795	295	183	435	0.834	2.28
IRF004	25	70	3.63	964	342	230	588	0.970	1.89

Working conditions of 3.0–5.0 kV accelerating voltage, a 10 μm aperture, and a working distance of 3–5 mm were used.

Insights into the development of microstructures in three dimensions were obtained using microcomputed X-ray tomography acquired using a micro–computed tomography (CT) apparatus (Varslot et al., 2011). Samples were imaged over a 360° rotation at 0.125° intervals, with differences in X-ray attenuation providing information on the distribution of various phases (quartz, epoxy and air-filled voids, and epoxy impregnated gouge) within the sample. Data were collected from two samples (MIS012 and MIS018) and corrected for optical and camera distortion. The data were reconstructed using a modified Feldcamp algorithm (Sakellariou et al., 2004) generating a 20483 voxel tomogram with a voxel size or resolution of 1.5 μm. The tomography data were visualized using Drishti 2.5 software allowing the creation of 3-D models of the fault zone (Limaye, 2012).

3. Experimental Results

3.1. Mechanical Behavior

3.1.1. Characterization of the Mechanical Properties of Fontainebleau Sandstone

Six intact samples of Fontainebleau sandstone were loaded until shear failure (Table 1). Three experiments (IRF001, 003, and 018) were undertaken at approximately the same confining pressure to assess repeatability. Mechanical response is characterized by an initial period of elastic loading with a slight inflection approaching peak stress, marking the onset of irreversible deformation involving intragranular and intergranular microcracking (Figure 2a). At peak differential stress values between 588 MPa and 964 MPa, throughgoing catastrophic brittle shear failure occurs, resulting in stress drops up to 588 MPa and displacements up to 1.04 mm. The large coseismic stress drop and displacement are attributed to the release of stored elastic strain from the apparatus into the sample at failure (Paterson & Wong, 2005). Following rapid slip, the constant axial displacement rate was maintained until approximately steady state sliding was achieved. At confining pressures ≥50 MPa, the fault zone produced by the failure is typically oriented between 24 and 26° to the bulk shortening direction. At lower confining pressures this angle is reduced, with values of 16–17° recorded for 15–30 MPa, respectively.

A failure or ultimate strength envelope has been constructed to estimate the coefficient of internal friction and cohesive strength of the Fontainebleau sandstone (Figure 2b). Assuming a linear envelope, the coefficient of internal friction is ~1.17 with a cohesive strength of ~81 MPa; these values fall outside the typical frictional and cohesive strength range for most intact rocks (Hoek, 1965; Jaeger, Cook, & Zimmerman, 2007), although high internal friction values have been recorded for other sandstones (Rutter & Hackston, 2017). Possible contributing factors to these unusually high values include (1) the structure of the low porosity quartz sandstone, which consists of very strong, interlocked, and well-cemented grains and/or (2) that the failure envelope may deviate from a linear Coulomb relationship at low confining pressures, suggesting that the applied linear relationship may overstate cohesive strength. However, over the range of differential stresses investigated during the current suite of experiments the linear relationship provides a good fit ($R^2 > 0.98$) and is used in analysis of the mechanical data (Figure 2c).

3.1.2. Reactivation of Existing Faults

Twenty-three variably oriented, fault reactivation experiments were undertaken at $P_c = 100$ MPa (Table 2) and 50 MPa (Table 3). Mechanical data show that for fault angles between 25° and 55°, the initial postyield

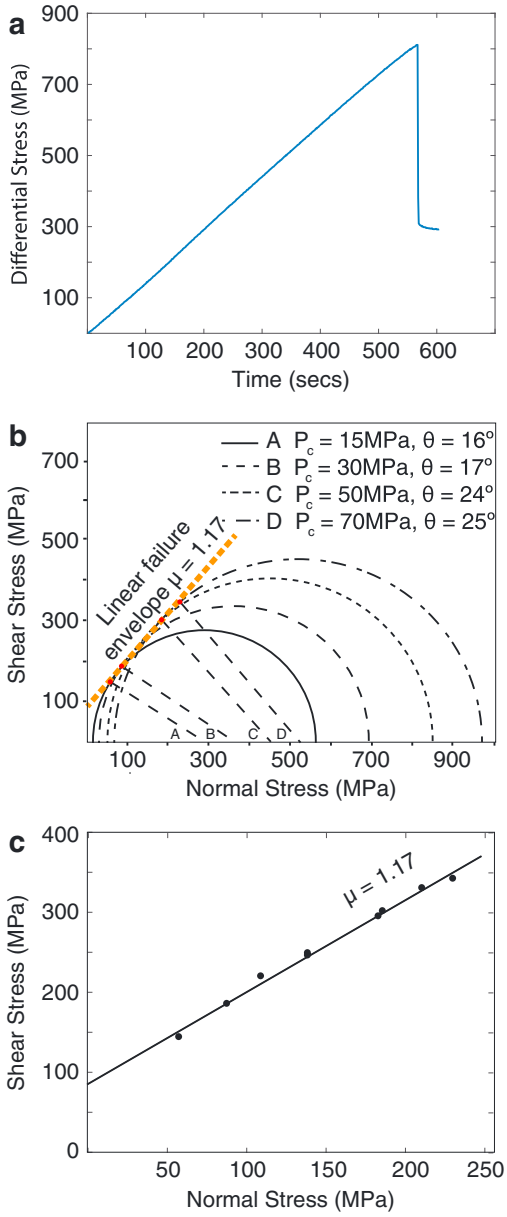

Figure 2. Mechanical results for intact rock failure experiments. (a) IRF018: representative loading curve for intact rock failure experiments. The large rapid stress drop represents the onset of strain localization and macroscopic failure of the specimen. (b) Failure envelope constructed using experimental data. The red circles represent stress conditions at failure. The dashed failure envelope assumes a linear relationship resulting in a large cohesive strength (~81 MPa) and internal friction (~1.17). It is likely that the failure envelope is nonlinear over a larger range of differential stresses. (c) However, for failure conditions considered in this study, the regime is well fitted with a linear correlation.

behavior of the samples is characterized by slip-hardening frictional sliding (Figure 3a). The yield point, which represents the onset of slip on preground interfaces, is often poorly defined, especially on more favorably oriented faults. In this study the yield point has been defined as the location of the initial deviation in gradient from approximately linear elastic loading. Following yield, as shortening increases, the sliding behavior transitions from a stable sliding regime into stick slip, where the fault episodically moves at fast slip rates after which there is a period of elastic reloading. Stable sliding behavior without a transition to stick slip occurs on favorably oriented faults (θ_r = 25°–35°) where P_c = 50 MPa. Experiments undertaken with a reactivation angle, θ_r = 60°, do not have a clear yield point, although there is a slight inflection on the stress-strain curve prior to the first slip event, possibly indicating the onset grain-scale microfracturing (Passelègue et al., 2016).

Changing the orientation of the ground surface from favorably to unfavorably oriented increases the peak normal stress acting on the fault. Consequently, the differential stress required to initiate slip increases. The magnitude of the stress drop and coseismic slip displacement accompanying macroscopic rupture also correlates with fault orientation, with larger stress drops (up to 340 MPa) and slip displacements (up to 1.26 mm) occurring on the more unfavorably oriented faults (Figures 3a and 3b). After the occurrence of a major stick-slip event (stress drop ≥20% peak differential stress) on unfavorably oriented faults where θ_r = 55° and 60°, the subsequent loading curves are consistent with nearly pure elastic loading followed by the onset of permanent deformation just prior to the second peak stress values. Subsequent macroscopic shear failure results in rupture localization on a new, approximately optimally oriented fault.

A failure envelope for the reactivation of preground surfaces has been constructed using the relationship between shear stress and normal stress at the yield point, assuming that the fault is cohesionless (Figure 3c). The gradient of the envelope provides an estimate of 0.54 for the coefficient of static friction. Although this value is lower than the experimentally determined friction coefficients of Byerlee (1978), it is consistent with previous experimentally derived values using the same sample preparation techniques and starting material (Cox, 1998). Following the onset of sliding, the coefficient of sliding friction increases with continued slip and is likely associated with changing asperity interactions and fault surface properties (Figure 3d) (Dieterich, 1979).

3.1.3. Estimating of Slip Velocities and Asperity Temperatures During Fast Slip

Using the data acquired with the interferometer, a lower bound on slip velocity has been estimated using a two-step process. First, the high-frequency ambient noise is removed by identifying a quiescent period before slip and using a hard wavelet thresholding approach. This approach suppresses high-frequency noise while preserving the character of the displacement signal, including any small episodic slip events. Next, it is assumed that the slip behaves, to a first order, as a logistic function. A function is fitted to the calibrated displacement data ($R^2 > 0.95$), and the derivative provides a lower bound on the estimated slip velocity (Hayward et al., 2016). Using this methodology, slip velocities of up to 41 cm s^{-1} are estimated for the events occurring during experiment MIS043 (Table 4).

Table 2
Fault-Reactivation Experiments Undertaken on Quartz Sandstone Interfaces at 100 MPa Confining Pressure

No.	Angle θ (deg)	Confining Pressure (MPa)	Axial disp. rate ($\mu m.s^{-1}$)	Peak diff. stress (MPa)	Peak shear stress (MPa)	Peak normal stress (MPa)	Stick-slip/ failure	No. of rapid slip events	Stress drop of largest slip event (MPa)[a]	Shear disp. of largest slip event (mm)[a]	Stress drop during failure of new fault (MPa)	Total exp. disp. (mm)	Comments
MIS005	25	100	3.63	425	163	176	Low amplitude stick slip	–	–	–	–	1.69	
BIS008	30	100	3.63	438	190	208	Yes	7	35	0.075	–	1.66	
MIS001	35	100	3.63	495	233	262	Yes	7	67	0.125	–	1.44	
MIS002	40	100	3.63	545	268	323	Yes	12	63	0.144	–	1.99	
MIS037	45	100	3.63	499	250	349	Yes	1	84	0.183	–	0.67	Halted after first major slip
MIS007	45	100	3.63	654	327	428	Yes	6	208	0.463	–	2.63	
MIS043	45	100	3.63	644	322	419	Yes	5	165	0.404	–	2.06	Interferometry
MIS003	50	100	3.63	770	379	548	Yes	3	340	0.892	–	2.25	
MIS006	55	100	3.63	1037	487	796	Yes	2	181	0.469	623	1.81[b]	
MIS038	60	100	3.63	934	404	804	Yes	1	227	1.260	–	1.37[b]	
MIS004	60	100	3.63	933	430	845	Yes	2	259	0.739	529	1.91[b]	

[a]Values given for largest reactivation on the preground fault. [b]Total experimental displacement is given as axial displacement rather than shear displacement due to the formation of a new optimally oriented fault.

Table 3
Fault-Reactivation Experiments Undertaken on Quartz Sandstone Interfaces at 50 MPa Confining Pressure

No.	Angle θ (deg)	Confining pressure (MPa)	Axial disp. rate ($\mu m.s^{-1}$)	Peak diff. stress (MPa)	Peak shear stres (MPa)	Peak normal stress (MPa)	Stick-slip/ failure	No. of rapid slip events	Stress drop of largest slip event (MPa)[a]	Shear disp. of largest slip event (mm)[a]	Stress drop during failure of new fault (MPa)	Total exp. disp. (mm)	Comments
MIS013	25	50	3.63	298	114	104	No	–	–	–	–	1.69	
BIS012	30	50	3.63	302	131	127	Yes	–	–	–	–	1.82	
MIS008	40	50	3.63	397	196	216	Yes	12	30	0.063	–	2.03	
MIS009	45	50	3.63	439	219	270	Yes	17	17	0.036	–	1.89	
MIS035	50	50	3.63	375	185	272	Yes	–	–	–	–	0.84	Halted prior to first major slip
MIS010	50	50	3.63	649	319	432	Yes	5	191	0.436	–	2.37	
MIS036	55	50	3.63	755	355	558	Yes	1	302	0.794	–	1.44	Halted after first major slip
MIS011	55	50	3.63	776	365	572	Yes	3	201	0.665	466	1.86[a]	
MIS031	55	50	3.63	787	370	579	Yes	3	284	0.738	391	1.98[a]	
MIS012	60	50	3.63	823	356	669	Yes	2	282	0.940	418	1.68[a]	
MIS017	60	50	3.63	591	256	494	Yes	1	152	0.297	–	0.53	Halted after first major slip
MIS018	60	50	3.63	827	358	671	Yes	1	309	0.561	–	1.09	Halted immediately prior to failure on new optimally oriented fault
MIS028	65	50	3.63	788	394	445	Yes	1	–	–	505	1.27[a]	
MIS029	70	50	3.63	802	401	452	Yes	1	–	–	540	1.48[a]	

[a]Values given for largest reactivation on the preground fault. [b]Total experimental displacement is given as axial displacement rather than shear displacement due to the formation of a new optimally oriented fault.

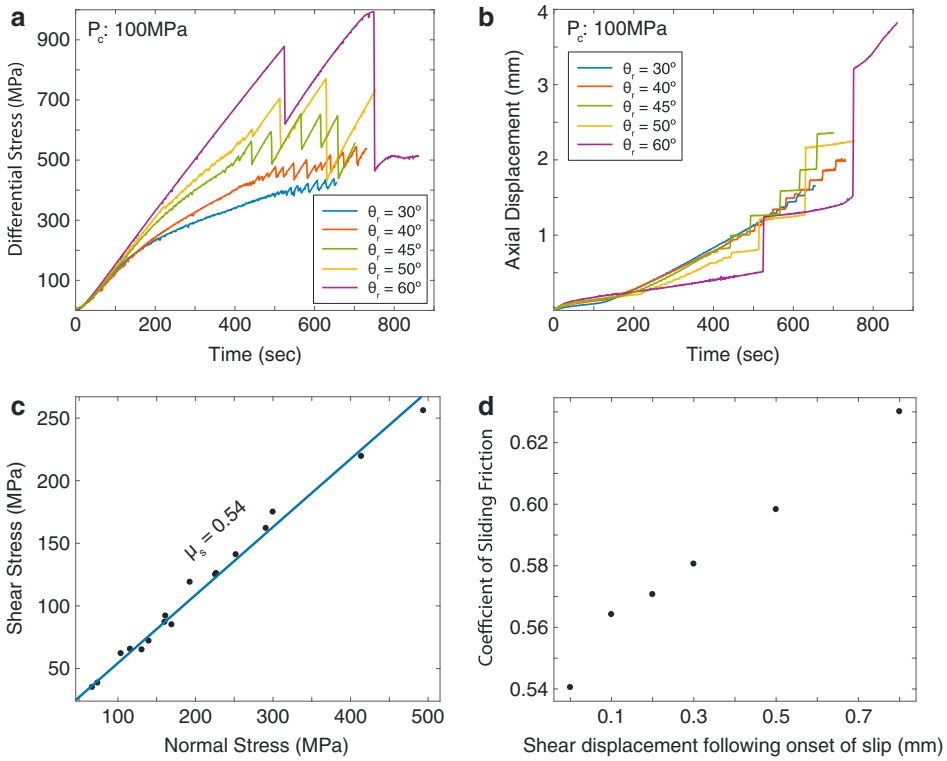

Figure 3. Mechanical results for fault reactivation experiments. (a) Representative loading curves for a series of misoriented fault experiments undertaken at P_c = 100 MPa. Experiments show how sliding behavior changes as the fault reactivation angle is increased from 30° to 60°. (b) Shear displacement is shown as a function of time during the slip experiments. With increasingly unfavorable fault orientations the size of the episodic rapid slip events increase. (c) The relationship between shear stress and normal stress is used to estimate the coefficient of sliding friction at the onset of slip. (d) Sliding friction values have been calculated using data from a number of experiments (θ_r = 25–55°). A reactivation envelope, constructed in the same manner as Figure 3c, is used to estimate the coefficient of sliding friction at each displacement increment. Data are only used until the onset of stick-slip behavior. The coefficient of sliding friction increases in an approximately linear manner with increasing slip displacement, possibly reflecting the evolution of the slip surface.

Frictional heating at grain-scale asperities has been estimated using a flash heating model (Brantut & Platt, 2016; Rice, 2006). Given that slip distance can far exceed the potential length of two grains in contact, the maximum asperity temperature has been calculated based on an estimated contact distance (D) of half the average diameter of a Fontainebleau grain or approximately 75 μm. If asperities are assumed to interact for the duration of the potential contact, time (t) is estimated by

$$t = \frac{D}{V} \tag{2}$$

Table 4
Fault-Reactivation Experiment Undertaken With Interferometer to Record Displacement During Fast Slip Events

No.	Rapid slip event	Angle θ (deg)	Confining Pressure (MPa)	Axial disp. rate (μm.s^{-1})	Peak diff. stress (MPa)[a]	Peak shear stress (MPa)[a]	Peak normal stress (MPa)[a]	Displacement during rapid slip (mm)	Peak slip velocity (cm.s^{-1})	Stress drop (MPa)	Modeled max. asperity temperature (°C)[b]
MIS043	1	45	100	3.63	424	212	309	0.093	6	37	891
MIS043	2	45	100	3.63	555	277	375	0.316	31	128	1,993
MIS043	3	45	100	3.63	644	322	419	0.404	41	165	2,288
MIS043	4	45	100	3.63	615	307	405	0.370	36	151	2,146
MIS043	5	45	100	3.63	560	280	377	0.295	30	120	1,961

[a]Peak values of differential, shear, and normal stress prior to each slip event. [b]Maximum asperity temperature assumes that asperity contact is limited to a maximum of half the average grain size or approximately 75 μm.

where V is the experimentally derived slip velocity. Maximum asperity temperature can then be calculated as

$$T_{max} = T_{amb} + \frac{\tau_c V}{\rho c}\sqrt{\frac{t}{\pi\kappa}} \quad (3)$$

where T_{amb} is the experimental ambient temperature, in this case approximately 25°C; τ_c is the estimated asperity strength, estimated to be 10% of the shear modulus (~3.1 GPa (Rice, 2006)); ρc is the heat capacity per unit reference volume, estimated to be 2.87 MPa/°C for quartz; and κ = 2.23 mm^2 s^{-1} is the thermal diffusivity of quartz. Localized temperatures of up to 2,288°C are estimated, far exceeding the equilibrium melting temperature of quartz and consistent with the sheared glass textures discussed in section 3.2.2.

3.2. Microstructures

In this section we first describe the internal structure of fault zones produced by shear failure in intact Fontainebleau sandstone. These fault zones are then compared with the structures associated with reactivation of preexisting, unfavorably oriented faults. Finally, we examine the microstructural development of new, favorably oriented faults produced during ongoing sample shortening subsequent to frictional lock-up of unfavorably oriented faults.

3.2.1. Intact Rock Failure

3.2.1.1. Fault Geometry and the Damage Zone

The microstructure of the fault zone produced during a single failure event in the intact rock samples is characterized by an intense, relatively high displacement, cataclastic deformation zone that defines a fault core that is ~200–300 μm wide after 600–970 μm of slip. The fault core, or principal slip zone, is fringed by a more diffuse and irregularly distributed zone of relatively low displacement fracture damage up to a width of approximately 1 mm. At the sample scale the principal slip zone has a mildly undulatory structure (Figures 4a and 4b). In some samples multiple slip surfaces and conjugate faults develop, possibly reflecting the bulk experimental stress state in which $\sigma_2 = \sigma_3$.

The diffusely bounded fracture damage zones contain numerous intragranular and intergranular extension fractures, many oriented subparallel to the sample shortening direction. Along the fault zone and coinciding with dilational quadrants (Figure 5), subparallel arrays of intergranular dilatant cracks have formed at a high angle (60°–90°) to the principal slip zone. These fractures are up to 2–3 mm in length. Occasional shear fractures also develop, forming secondary fault strands subparallel or conjugate to the principal throughgoing fault (Figures 4a and 4b).

The undulatory nature of the main slip zone results in a strongly heterogeneous stress field (Chester & Chester, 2000; Griffith et al., 2010). Stress concentrations associated with contractional zones are interpreted to contribute to the development of secondary fault strands, forming what are effectively bypass structures. There is also evidence for the formation of fracture damage resulting from the transient changes in the stress field associated with strain accommodation during rupture. Arrays of dilatant fractures form approximately perpendicular to the tip of the propagating shear fracture. These extension fractures are interpreted to form in the dilatant quadrant of the developing fault as the rupture propagates dynamically (Figures 4a and 4b).

3.2.1.2. The Geometry and Microstructures of the Fault Core

The fault core is characterized by cataclastic deformation microstructures including extensively fractured grains and the formation of fault gouge. This highly angular and typically poorly sorted gouge consists of fragments ranging in diameter from submicron particles to remnant fractured grains up to approximately 100 μm in diameter. Narrow zones (width $<$ 5 μm) of slip localization occur as bands of very fine grained gouge both parallel to, and inclined to the fault boundary, forming Y-shears and Riedel shears, respectively (Logan et al., 1992; Passchier & Trouw, 2005).

The specimen-scale undulatory nature of the fault path forms both dilatant and contractional areas during slip. Dilatant, high-porosity zones form in jogs, or releasing zones, and are filled with large, angular fragments that are minimally rotated compared with the gouge in the principal slip zone. Dilational zones have widths of 200–300 μm and lengths up to 2 mm. In contrast, contractional zones are characterized by narrow slip zones (10–40 μm wide), fine gouge particles, and the formation of glass resulting from friction-induced melting of the quartz host rock. Zones of quenched melt are generally between 1 and 2 μm wide and up to approximately 200 μm in length. Although the melt has rapidly quenched to form a silica glass, we use

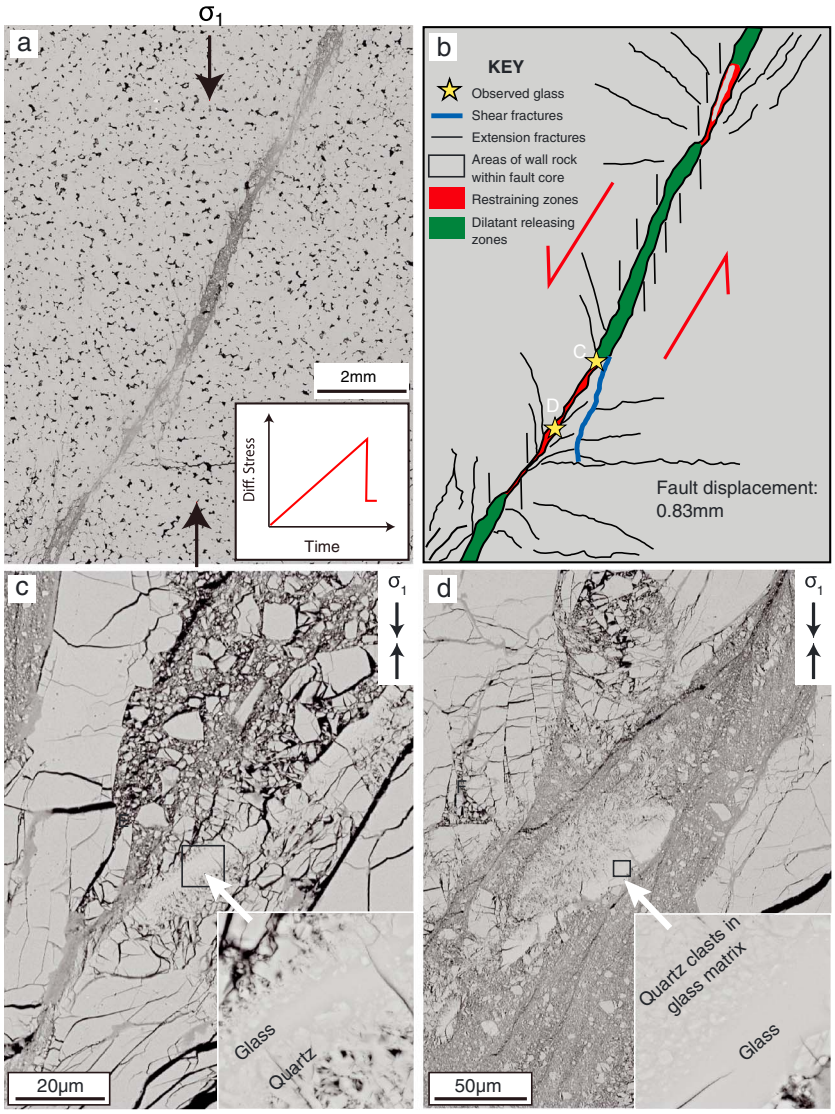

Figure 4. Microstructures produced during failure of intact rock. Experiment IRF001; backscattered electron-SEM images of the epoxy impregnated samples. (a) Overview of the sample following deformation. Axial loading direction indicated by the black arrows. Inset: schematic loading curve for the experiment. A 200–300 μm wide failure zone is evident, and (b) an interpretative diagram is provided. Undulatory nature of the failure zone results in development of dilatant and compressive zones. Secondary fault traces develop around some compressive regions along with the formation of glass produced by frictional heating (see stars at locations C and D). (c and d) Axial loading direction is indicated. Images showing the morphology of the glass produced within the fault core as indicated in (B). Note the sharply defined generation surface on one side of the glass zone. Insets show a high magnification view of the glass in areas identified on the main image.

the terms "glass" and "frictional melt" interchangeably to describe the textures and highlight the processes involved in formation.

The glass is most easily identified where relict quartz clasts are suspended within a solid glass matrix (Figures 4 and 6). At low magnifications during BSE-SEM imaging, quenched melt is recognized by the presence of elongate bands of bright material within the fault core; these bands typically have at least one sharply defined edge (Figures 4c and 4d). The melt zones are less porous than the surrounding fault gouge. Accordingly, during low magnification BSE-SEM imaging, they appear bright compared with epoxy-impregnated gouge. At higher magnifications, the glass is recognized by having slightly lower electron intensity than intact quartz (Figure 6). This is interpreted to result from either a lower orientation contrast from a nonuniform reflection of low-loss BSEs in the noncrystalline structure or a reduced Z contrast (representing mean atomic number) due to the lower density of the glass compared with its crystalline equivalent. The

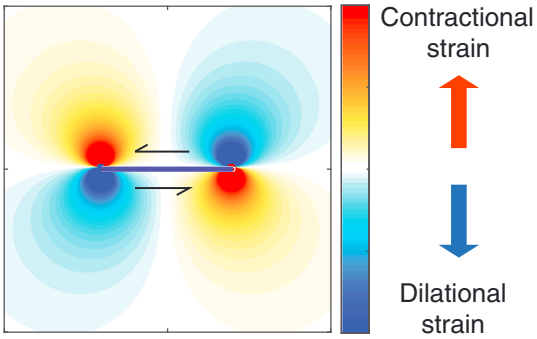

Figure 5. Quadrants of dilational and contractional strain following fault slip. Model was produced using Coulomb 3.4 (Toda et al., 2011). The fault is represented as a dislocation within a uniform elastic half space. Dilational strain quadrants are associated with the formation of dilatant features such as extension fractures while fracturing in the contractional quadrant is often suppressed.

amorphous structure of this material has been confirmed using transmission electron microscopy (Hayward et al., 2016).

Although the volume of melt produced during slip varies greatly between experiments, it remains a minor component (<5% of the cross-sectional area) of the newly formed fault zone. Two styles of melt zones are recognized in cross section: (1) glass bands with a sharp, planar boundary on one side, grading progressively into a melt-indurated gouge on the other side (Figures 4c and 4d and 6d), and (2) short melt "-veins" between two impinging asperities (Figures 6a and 6b). Radiating Hertzian-style fractures at these sites are indicative of high stress concentrations. Some glass regions show the formation of banded textures, with repeated juxtaposition of clast-free principal slip zones against melt-indurated gouge (Figure 6c). This suggests that on the time scale of a single slip event (<1 ms), there can be multiple episodes of shear heating, melting, melt shearing, and quenching (cf. O'Hara, 1992; Spray, 1992).

3.2.2. Fault Reactivation Experiments

Fault reactivation experiments were undertaken to explore the development of fault zone fracture damage, frictional lock-up, and the generation of new faults using samples with preground faults oriented in 5° increments between 25° and 65° relative to the far-field maximum principal stress. With an increasing reactivation angle, the faults support larger peak normal stresses and their behavior transitions from stable sliding to increasing amplitude stick slip. Offsets of the copper jacket and microstructures formed within the core indicate that for experiments where $\theta_r \leq 50°$, reactivation occurs on the existing preground fault (Figures 7a).

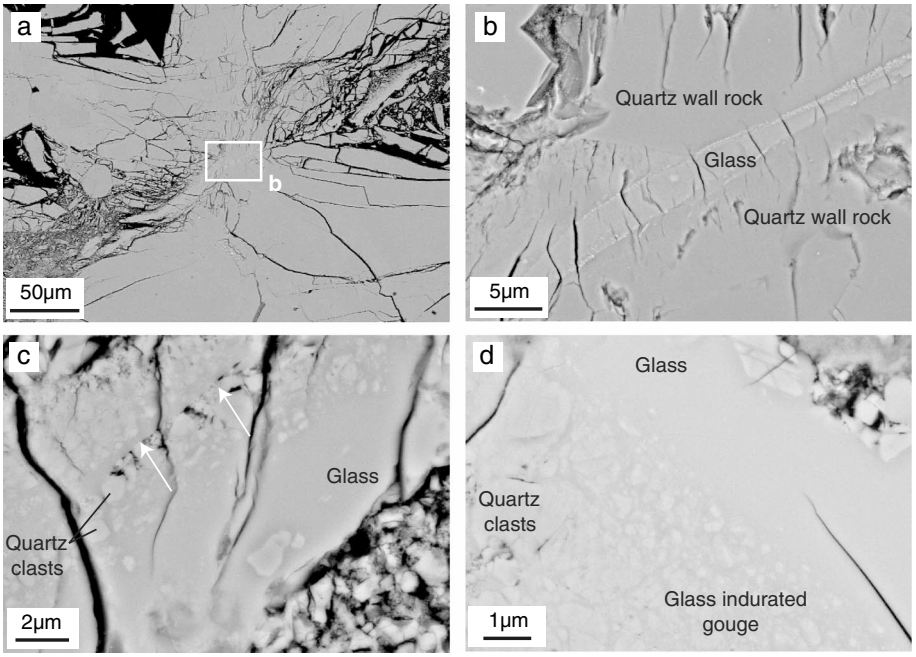

Figure 6. Glass microstructures formed during the failure of intact rock. (a–c) IRF018 and (d) IRF001; both experiments are nominally dry failures of intact rock. Highly stressed contact between two asperities on a fault surface formed during stress-driven failure (Figure 6a). Hertzian fractures can be seen radiating from the impinging contact and a layer of melt has formed at the interface. Higher magnification image of the 2–4 μm wide glass layer formed at the contact between asperities shown in Figure 6a (Figure 6b). Note the formation of "ladder" cracks in glass layer; these are possibly associated with anisotropy in the compressibility of the adjacent quartz. Banding within the 12 μm wide frictional melt layer indicates multiple episodes of melt formation during the single slip event (Figure 6c). The arrows point to a possible second melt generation surface. High magnification image of glass zone shown in Figure 4d (Figure 6d). The frictionally melted region contains a clast-free glass vein transiting into an area of increasing clast density with rounded clasts supported within a glass matrix. Moving further away from the generation zone angular fragments of quartz dominate but are glass-indurated.

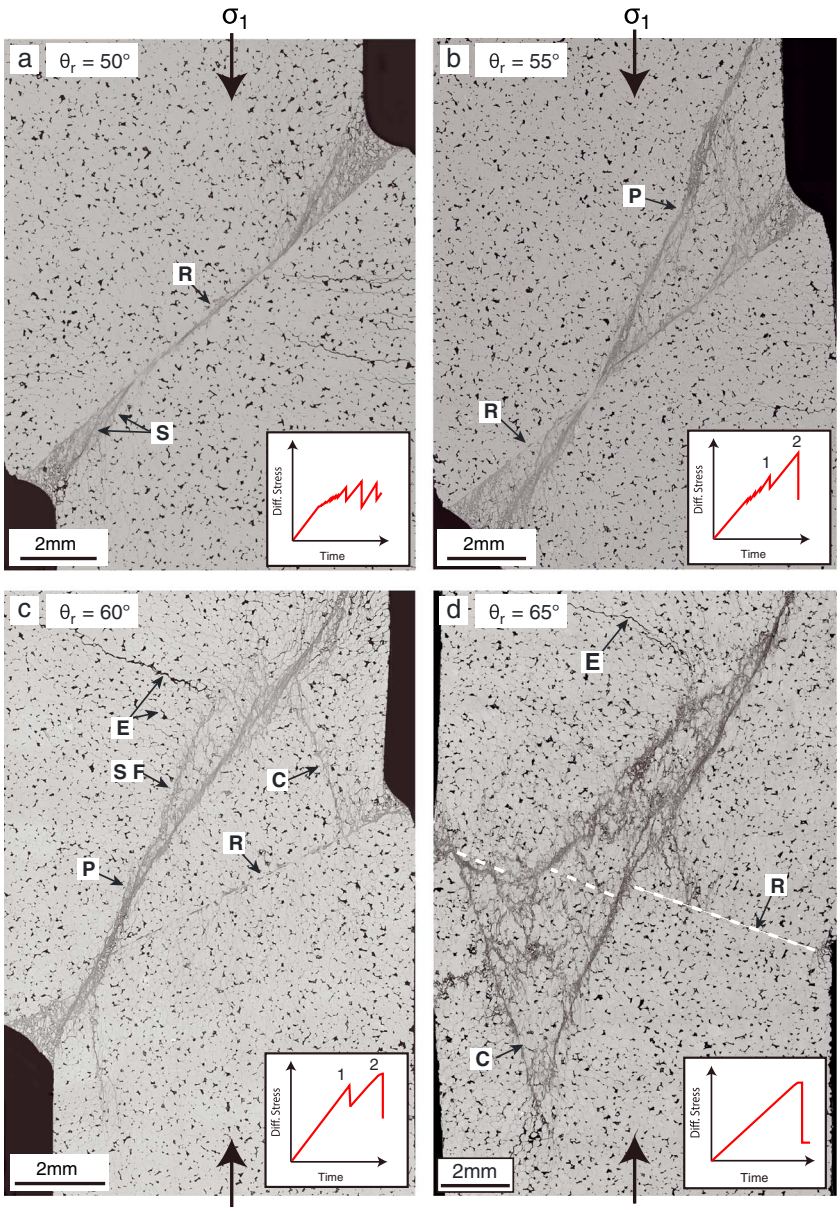

Figure 7. Sample scale microstructures produced by the reactivation faults of different orientations. BSE-SEM images showing an overview of microstructures formed during fault reactivation and failure over a range of reactivation angles (θ_r = 50–65°). Insets show a schematic loading curve for each experiment. All experiments undertaken at P_c = 50 MPa. Preground misoriented fault indicated by "R." (a) MIS010, θ_r = 50°, fault reactivates initially by slip hardening then transitions into stick-slip behavior. Fault shows development of splay-like fault traces at the fault ends, indicated by "S." (b) MIS011, θ_r = 55°, fault slip hardens then evolves into a stick-slip regime. On the second major slip event (indicated in the inset) the sample fails along a new, more favorably oriented fault. The footwall fracture resembles a splay-like fault, similar to those seen in A, but the hanging wall is bisected by a new primary fault trace, "P." (c) MIS012, θ_r = 60°, fault elastically loads and slips once on the misoriented fault, before reloading and failing on a new fault. Similar microstructures to (B), but note the formation of a secondary fault trace ("S F") and accompanying dilational cracks, "E" in the hanging wall. (d) MIS028, θ_r = 65°, preground surface indicated by white dashed line. This preexisting fault is frictionally locked and sample failure along a complicated network of newly formed faults after a period of nearly pure elastic loading. Conjugate faults are indicated by "C."

Faults oriented at 55° and 60° incur a major slip event on the unfavorably oriented fault before locking up. Upon reloading, failure occurs by the formation of a new near-optimally oriented fault (Figures 7b and 7c). Faults where $\theta_r > 60°$ do no reactivate; rather a new favorably oriented fault develops (Figure 7d). In the following section we outline how changes to existing fault orientation influences the development of

microstructures within the fault core and adjacent low displacement damage zone, leading to the lock-up of highly misoriented faults.

3.2.2.1. Sample-Scale Microstructural Evolution of Damage on Preground Faults

The cross-sectional microstructure of faults oriented at θ_r = 25°–30° is characterized by minimal damage and only rare intragranular microcracks. Increasing fault reactivation angles correlates with increasing lateral and near-fault fracture damage. Gouge formation and near-fault damage reach a peak on faults oriented at θ_r = 45°–50°. Splay-like fractures develop in dilatant zones (Figure 5) of fault ends in samples oriented at θ_r = 35°–50°, forming intergranular shear fractures up to 3–4 mm in length, at angles of 25°–45° to the preground fault surface. Following the single large slip event on preexisting faults where θ_r = 55°–60°, low displacement damage is limited to a zone approximately 200 μm wide, or about 1 grain width, on either side of the fault.

With an increasing reactivation angle, intragranular extensional microcracking also becomes more abundant. Extensional microfractures are preferentially located on the dilatant sides of the fault ends adjacent to, and between, the splay-like fractures. Microfracture orientations range from parallel to perpendicular to the fault surface with orientation being influenced by the location on the fault (i.e., proximity to the fault, near to the fault ends, or close to the center of the sample).

3.2.2.2. Evolution of the Fault Core in Samples With Preground Fault Surfaces

Reactivated fault cores range in width from $<$2 to 300 μm, with wider cores being associated with higher total displacement. Fault cores that have experienced multiple rapid slip events or stable sliding $>$1 mm are dominated by the presence of fractured grains and fault gouge. In samples that have slipped by stable sliding, there is evidence for the development of slip localization structures such as Riedel shears. As the reactivation angle increases the process of gouge formation transitions from high displacement damage, produced by wear and the attrition of asperities, to being largely low displacement damage, resulting from intense grain crushing and fracturing (i.e., pulverization; Reches & Dewers, 2005).

An important microstructural characteristic of fault zones that have failed by episodic rapid slip is the presence of glass generated by frictional melt. The quenched melt forms a heterogeneously distributed layer along the slip surface that, in places, forms a continuous glass layer between the two surfaces, welding segments of the fault (Figures 8a and 8c). Frictional melt is recognizable on the fault surface by the formation of drawn-out, ribbon-like filaments of glass (Figure 8d). In cross section the melt origin of the welded zones is indicated by the presence of elongate, strained vesicles and heterogeneous propagation of the melt front into adjacent wall rock, forming an uneven melt substrate boundary and the appearance of submicron-sized melt injection veins (Figure 8a). Increasing confining pressure and/or reactivation angle increases the prevalence of melt welding, with fault surfaces transitioning from localized melting at asperity contacts where $\theta_r \leq 40°$, to the development of semicontinuous melt layers between θ_r = 45°–50°. On faults where $\theta_r \geq 55°$, essentially every grain contact is welded by a thin layer of melt.

The formation of melt has a notable impact on the subsequent development of microstructures within the sample. Intragranular and grain boundary fractures commonly form in the quartz grains adjacent to the melt-welded sections. Fracture development is likely enhanced by both the large thermal stresses resulting from temperature gradients and anisotropy of thermal expansion coefficients in the wall rock adjacent to the melt and also by high stresses at interacting asperity contacts. Splays nucleate from or are spatially associated with sites of melt welding (Figure 9). Splay-like shear fractures develop at the fault ends, bypassing the welded zone, forming a more favorably oriented fracture (Figures 9a and 9b). With continued slip, fault movement is increasingly accommodated on the new fractures forming secondary faults.

3.2.3. Evolution and Structure of New Favorably Oriented Faults

The appearance and morphology of new favorably oriented faults (that form following frictional lock-up of unfavorably oriented faults) is similar to that of faults produced during intact rock failure experiments. The fault zone is undulatory, resulting from linkage of en echelon fault segments, and the development of secondary fault traces (Figures 7b and 7c). Fault planes that are conjugate to the main slip zone also form, although these accommodate minimal displacement (Figure 7c). Overprinting relationships between the conjugate faults indicates the contemporaneous formation of the two fault sets.

The development of new faults has been explored using a series of experiments that were halted at various stages within the rupture sequence (Figure 10). MIS017 θ_r = 60° was halted immediately after the first

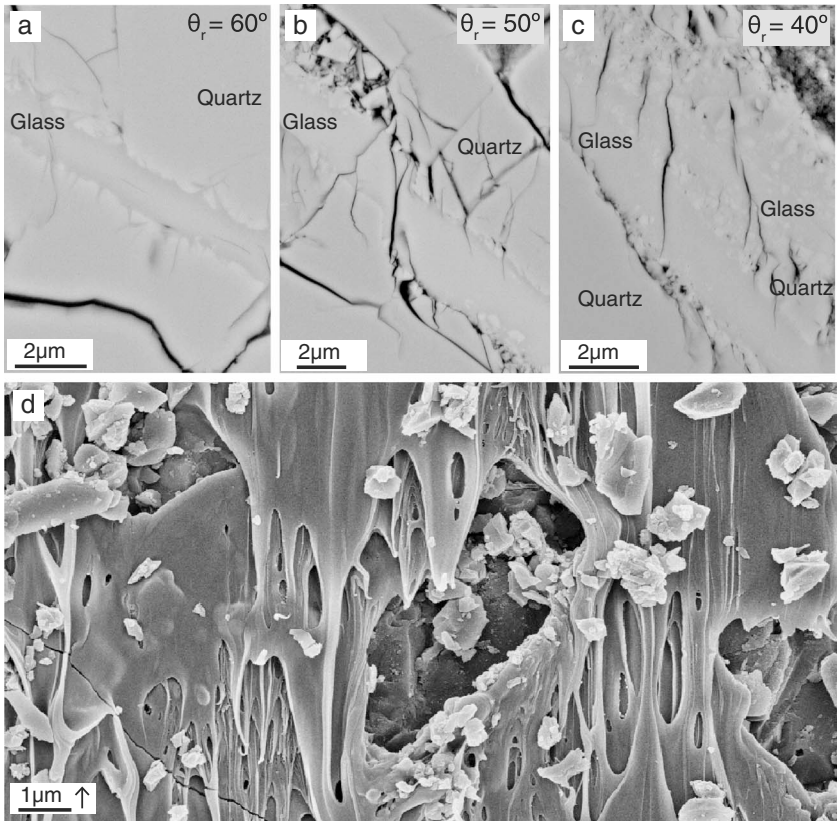

Figure 8. Frictional heating, melting, and melt welding. (a–c) BSE-SEM images taken perpendicular to the reactivated faults and parallel to the direction of slip. Veins of quenched melt weld areas of the existing fault surfaces (θ_r = 40–60°). With a decreasing reactivation angle (θ_r), glass becomes highly localized at asperity contacts. Banding of the melt layers between layers of clasts indicating multiple melt generation events (Figure 8c). (d) Secondary electron scanning electron microscopy (SE-SEM) image of the slip surface. The black arrow accompanying the scale bar indicates the orientation of slip of the imaged fault block. Sheared glass forming filaments indicates frictional melting on the slip surface.

slip event on the unfavorably oriented fault, and MIS018 θ_r = 60° was halted at the second peak in stress, just prior to macroscopic failure on a newly developing, favorably oriented fault. At the sample scale, microfracture damage in MIS017 is limited to approximately a single grain width (250 μm) on either side of the preground slip surface with a small amount of damage evident at the fault tips (Figures 10a and 10b). Within the fault core, all grain to grain contacts are welded by a layer of frictional melt (Figure 10c).

Reloading after the first slip event results in a marked increase in fracture density and a widening of the damage zone surrounding the preexisting θ_r = 60° fault (Figure 10d). The distribution of microfractures is not pervasive throughout the sample, but rather, forms around the original fault surface and in a zone that coincides with where the new fault forms. Large areas of the sample remain essentially damage free.

The new favorably oriented fault forms by the interaction and coalescence of extension fractures that localize at the propagating fault tip (Figure 10f) (Lockner et al., 1991). The localization of damage occurs over a width of approximately 250 μm. Even before macroscopic failure occurs that would result in a large stress drop, significant shear strain has been accommodated on the newly growing fault zone. The original θ_r = 60° fault is offset by ~200 μm where it is intersected by the developing fault (Figure 10e). Intergranular extension fractures develop perpendicular to the newly forming fault in the dilatant quadrant of the fault tip. The location and dilatancy of these fractures suggest that strain was also accommodated at the fault tip and may contribute to the propagation of the new fault (Figure 10f). Despite the accommodation of strain on the newly developing, favorably oriented fault, there is no evidence of frictional melting within the fault core, highlighting the role of slip velocity in the generation of frictional heat.

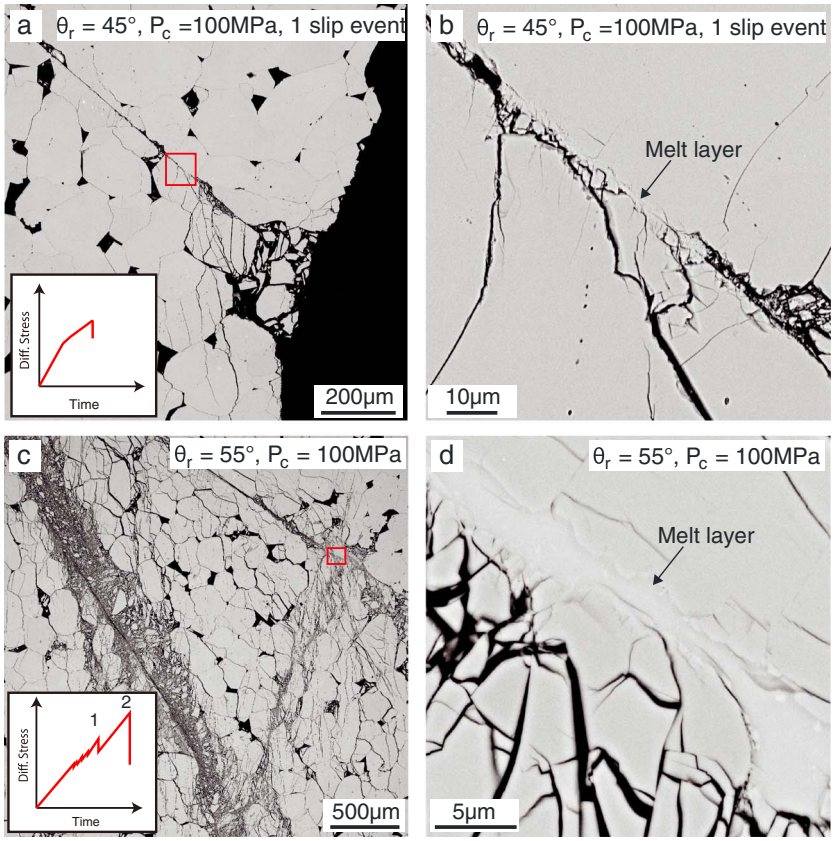

Figure 9. Melt welding and its influence on the microstructural evolution of the fault surfaces. Secondary fault traces initiate from sites on reactivated faults that are melt-welded, suggesting that quenched melt influences the microstructural evolution of the fault surface. (a and b) MIS037; fault damage zone microstructures after a single rapid slip event. Fractures develop from the melt-welded sections forming splay-like damage zones at the fault tips. (c and d) MIS006; conjugate fault linking the existing fault and the new more favorably oriented fault nucleates from a melt-welded zone. The red rectangle shown in c bounds the area of the higher magnification image (Figure 9d). Note that in both high magnification images (Figures 9b and 9d), damage initiates in the wall rock adjacent to the melt zone, rather than within the quenched melt.

3.2.3.1. Microstructures of Fault Cores and Formation of Melt in New Favorably Oriented Faults

The structure of the core of new faults, analyzed following macroscopic failure during reactivation experiments, is similar to those produced during intact rock failure. However, in contrast to the intact rock failure experiments, where formation of melt is rare and largely constrained to compressional zones within the fault core, new faults formed during reactivation experiments produce extensive bands of frictional melt that are up to 1.2 mm long and 20 μm wide. These melt zones are generally characterized by one approximately planar surface, interpreted as the melt generation plane, and a melt zone that grades into a more porous region of melt-indurated gouge. Wall rock adjacent to the melt layer typically is extensively fractured, commonly to the point of pulverization, where grain shattering is so intense that particles are submicron in size. Mosaic-like clast textures indicate little shear strain in these areas. The melt layer, however, remains largely intact.

3.2.4. 3-D Quantification of the Spatial Extent of Melt Welding on Fault Interfaces

High-resolution microcomputed X-ray tomography has allowed nondestructive investigation of the internal features of melt-welded samples in 3-D. The essentially single-phase mineral composition of the Fontainebleau sandstone creates a bimodal X-ray attenuation distribution based on the average density of any given volume or voxel. The density contrast between the quartz grains and epoxy/air-filled voids has enabled separation of tomographic data into pore and mineral phases, allowing three-dimensional visualization of damage associated with fault rupture.

Individual voxel density information has been used to segment the data set, allowing colors to be assigned to the different phases. Unlike open fractures that have a high-density contrast with the surrounding quartz,

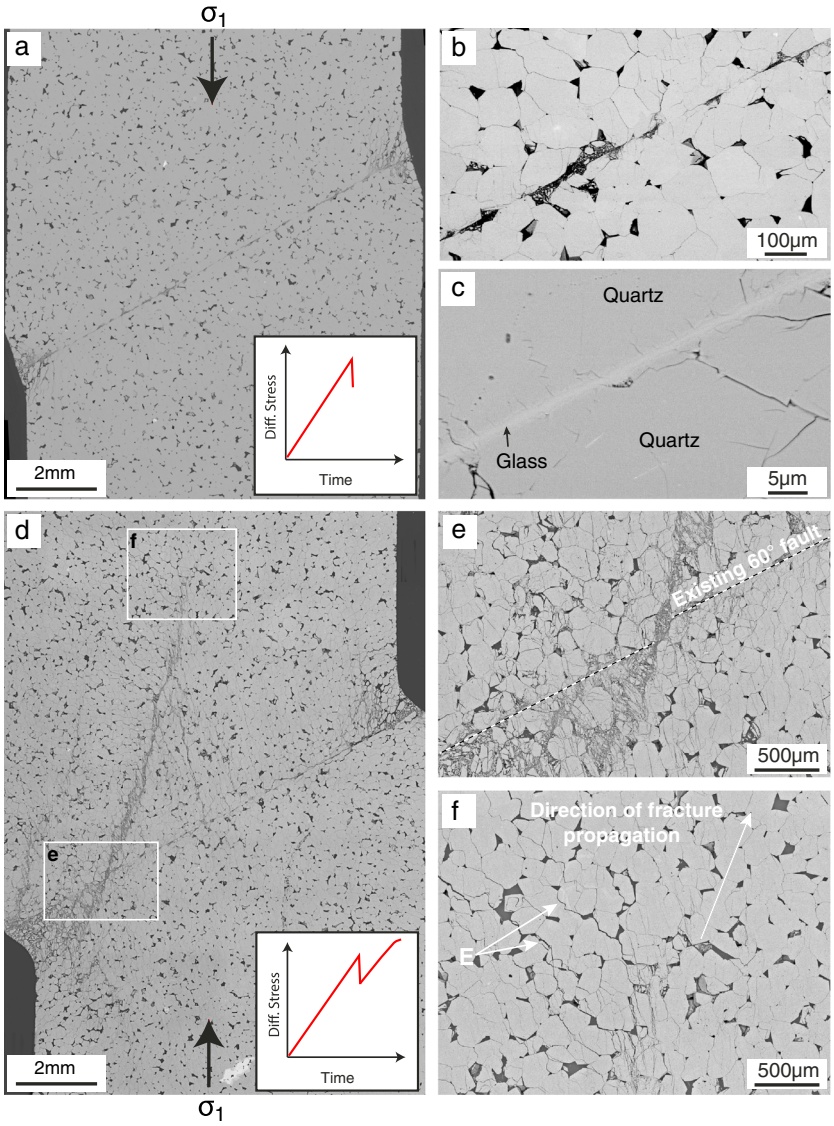

Figure 10. Formation of a new optimally oriented fault following frictional lock-up on a θ_r = 60° fault. (a–c) MIS017; experiment halted immediately following the first slip event. Inset: Schematic loading curve. BSE-SEM montage of entire sample (Figure 10a). Cross-section cut perpendicular to the fault surface and parallel to the slip direction. Damage zone is poorly developed with minor intergranular fractures and grain crushing (Figure 10b). Intragranular fracturing is largely confined to approximately 200 μm on either side of the fault surface. Main deformation feature of the fault core is melt welding of grain to grain contacts (Figure 10c). (d–f) MIS018; experiment halted at the onset of macroscopic shear failure along a newly formed fault. The new fault is in the process of forming and, when compared with MIS017, significant damage is present. Although the fault zone is not fully developed, shear strain has been accommodated along the developing fault. Accommodation of strain results in the offset of the preground fault (indicated by the dashed lines) (Figure 10e) and through the formation dilatant fractures at the fault tip – Indicated by "E" (Figure 10f).

glass formed by frictional melting has the same atomic composition and similar density. This means that melt-welded regions do not significantly alter the attenuation of X-rays during scanning; rather the fault zone in melt-welded regions is invisible between the adjacent quartz grains. For a thin slice of tomography data (50–75 μm on either side of the fault surface), the segmented data associated with the quartz are made transparent allowing visualization of the spatial extent of the frictional melt. Any transparent region across the fault zone represents areas where the grain interfaces are frictionally welded, forming a continuous quartz-silica glass transect through the imaged section (Figures 11a and 11b). The validity of this assumption has been tested using BSE-SEM imaging of a region from the same sample and

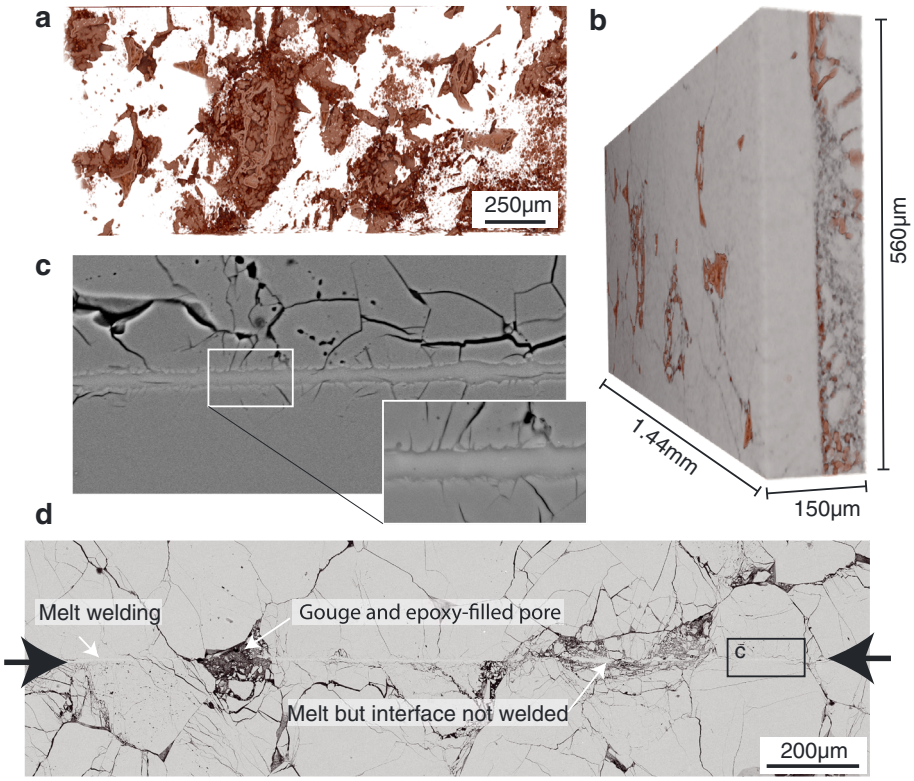

Figure 11. Spatial extent of melt-welding in 3-D. Experiment MIS018. (a) X-ray tomography image where the quartz phase is transparent. The white zones represent areas where grain interfaces are frictionally welded, producing continuous SiO_2 through the full depth of the imaged section. The brown regions represent fractures, gouge, and pores with a lower density. (b) 3-D view of the imaged volume shown in Figure 11a. (c and d) BSE-SEM images of a two-dimensional transect made through the sample used in Figures 11a and 11b. Melt welding is evident between all grain contacts (Figure 11c). A larger area showing the fault zone structure and thin melt layers between grain contacts (Figure 11d). The black arrows indicate fault slip surface.

shows melt welding at every quartz-quartz interface across the slip surface (Figure 11c). This method does, however, underestimate the volume of melt that is produced, as it does not recognize areas where melt has formed and been displaced to a position adjacent to a pore space.

Although there is likely to be significant heterogeneity in the extent of melt welding within the sample, due to factors such as the formation of fracture damage zones at the fault tip, the micro-CT data allow quantification of the minimum 3-D spatial extent of the melt. Image analysis using Image J indicates that a minimum of approximately 48% of the fault is melt-welded.

4. Discussion

With increasing reactivation angle the mechanical behavior of experimental fault interfaces evolves from creep, through increasing amplitude stick slip (with rapid displacements of up to ~500 μm), to frictional lock-up and the generation of a new favorably oriented fault. The varying mechanical behavior is accompanied by changes in microstructural development, ranging from the development of millimeter-scale, low displacement fracture damage zones to melting and cataclasis on submicron scales within the high displacement fault core. Importantly for understanding the evolution of mechanical behavior, microstructural analysis demonstrates that the generation of frictional melt during rapid slip events significantly alters the fault processes through "melt welding." Heterogeneous welding within the slip zone is spatially associated with intense lateral fracture damage resulting from stress concentration around welded patches.

In the following section we outline a number of illustrative stress and strain models calculated using Coulomb 3.4 (Toda et al., 2011). These simple models are used to highlight small-scale heterogeneities in elastic strain and stresses, which result from melt welding and changes in fault geometry. The models consider faults as

dislocations within an infinite elastic half space with specified elastic properties (Young's modulus of 36 GPa (David et al., 2013) and Poisson's ratio of 0.16 (Pimienta, Fortin, & Guéguen, 2016)) and a coefficient of static friction as indicated by our experiments (μ_s = 0.54). A melt-welded fault is modeled as a series of aligned dislocations where the dislocations represent unwelded surfaces. Changes in fault geometry are considered at the sample scale as a series variably oriented dislocations representing active faults with simplified geometries. Although these models represent a significant simplification of processes within the sample, they do provide a fundamental understanding of the interplay between stress, strain, and microstructural development.

4.1. Melt Welding, Rheological Asperities, and the Formation of Off-Fault Damage

An important microstructural aspect of this study is the effect of melt-derived glass on the properties and evolution of the fault and surrounding damage zone. Melt-derived glass occurs on every fault interface that has experienced episodic rapid slip with coseismic stress drops $\gtrsim$60 MPa. At more favorable reactivation angles (i.e., $\theta_r \leq 40°$) and low confining pressures (P_c = 50 MPa), the development of melt is sporadic reflecting the lower normal stresses, with discontinuous regions of melt forming mainly at grain scale-asperity contacts. With increasing fault misorientation, progressively higher peak normal stresses are accompanied by larger displacement stick-slip behavior, an increasing volume of frictional melt and a growing proportion of the fault interface being welded. At reactivation angles $\theta_r \geq 55°$, most grain-to-grain contacts are separated by a layer of glass, welding up to 50% of the fault surface. These melt-welded contacts form patches of glass along the fault surface that are continuous over distances up to approximately 1 mm. In the next section we discuss how the formation of frictional melt on the fault surface (1) influences wear processes and the formation of off-fault damage, (2) increases cohesive fault strength, and (3) results in the generation of new, optimally oriented faults.

Little fracture damage occurs on unfavorably oriented preground faults until after the first rapid-slip event. During fast slip events, interfaces frictionally melt, leading to welding of grain-to-grain contacts and localized segments of the fault upon cessation of slip (Figures 12a–12c). If the fault is subjected to continued loading, stress concentrates at the ends of melt-welded, locked regions (Figure 12c). Fractures form in dilational quadrants (Chester & Chester, 2000; Griffith et al., 2010). In regions close to the fault ends (near the intersection of the test material and the surrounding metal jacket), both extension and shear fractures nucleate. Shear fractures develop at more favorable orientations, forming splay-like secondary fault traces. Subsequent fault slip is more readily accommodated on the newly developed shear fractures rather than the melt-welded, preexisting slip surface (Figures 12d and 12e).

Toward the center of the sample, fracturing around previously melt-welded zones forms subparallel to the misoriented fault, bypassing the welded zone (Figures 12f and 12g). Formation of these fractures is potentially enhanced by thermal cracking resulting from the large temperature gradient and rapid temperature changes in the wall rock adjacent to the welded zones. Chester and Chester (2000) showed that locally inhomogeneous stress states along faults result from variations in fault plane geometry leading to the formation of fractures that locally range in orientation from parallel to perpendicular to the fault plane. Bypassed melt-welded zones adhere to the opposite fault surface forming geometric asperities.

In the engineering community, the transfer of material from one surface to another is widely referred to as adhesive wear. Although there are a number of mechanisms that cause adhesive wear, the formation and rupture of locally welded asperities between rubbing surfaces is an important mechanism (Bowden & Tabor, 1950; Kerridge, 1955). Depending on the material and conditions, localized welding-induced transfer of material from one side of a slip surface to another is primarily responsible for the onset of surface degradation and the formation of wear debris in metals (Bowden & Tabor, 1942; Childs, 1980; Kerridge, 1955). In the current experimental example involving quartz interfaces, similar observations were made. Wear including commination and localized fracture damage is more pronounced following asperity welding. Subsequent slip bypasses the welded asperities resulting in the transfer of material from one side of the fault to the other, forming new asperities with an indenter-like geometry. Abrasive wear processes, such as asperity plowing, grain comminution, rotation, and translation then contribute to the formation of gouge within the fault core.

4.1.1. Continued Reactivation and Fault Maturation

With continued reactivation fault zones mature. Wear within the principal slip zone and the development of surrounding low displacement facture damage contributes to the mechanical evolution of the fault by

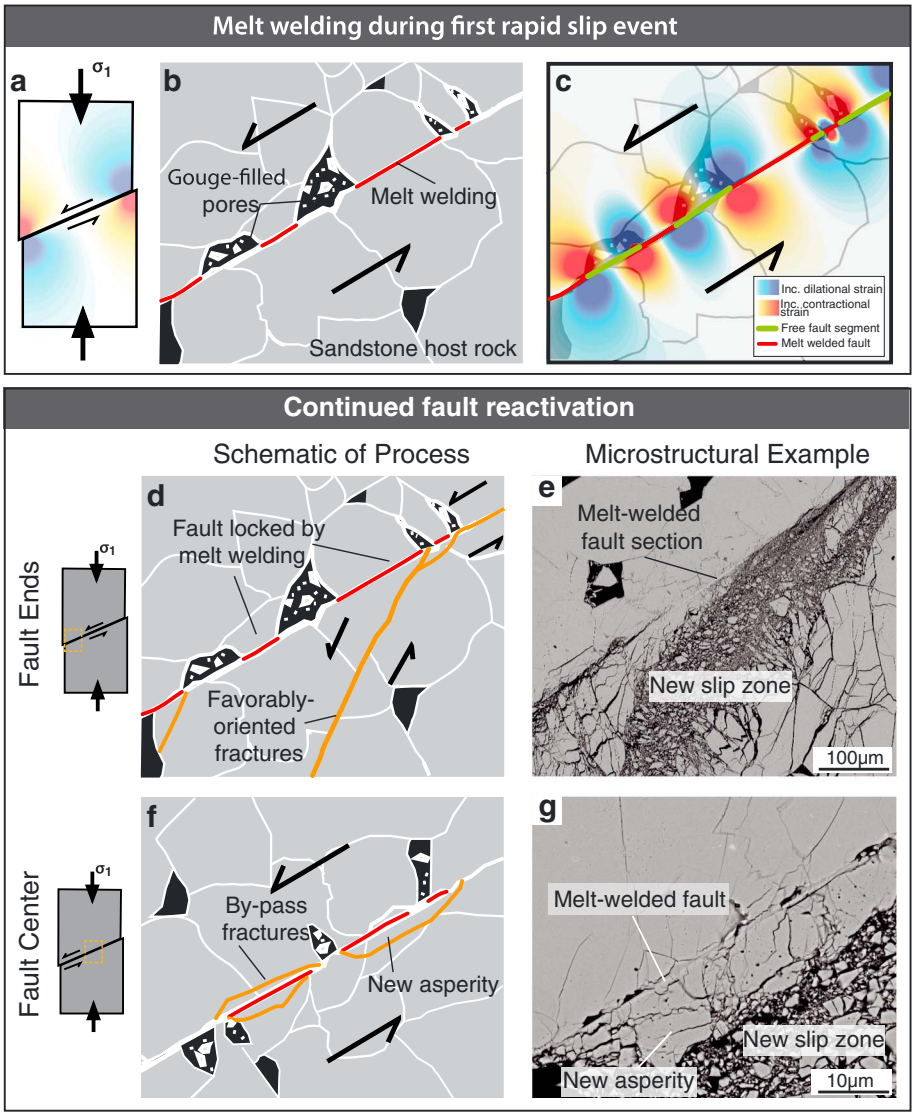

Figure 12. The role of melt welding in the formation of off-fault damage. (a) Dilatant (reds and yellows) and contractional zones (blues) within the sample. (b) During initial rapid slip events, frictional melt welds many quartz-quartz grain contacts. (c) The geometry of the faults shown in Figure 12b has been used to calculate elastic strain following slip to highlight heterogeneity resulting from melt welding. Model output has been superimposed on the original diagram for illustrative purposes. Note that the effects of pore geometry, grain boundaries, and the influence of a viscous melt have not been considered. (d–g) Continued reactivation of the fault results in the formation of damage. (At the fault ends melt-welded zones result in the formation of more favorably oriented fractures that accommodate continued slip (Figure 12d). The original slip surface is locked and deactivated (Figure 12e). In the center of the fault, fault-parallel shear fractures bypass the melt-welded zones (Figure 12f). When the fractures form in the wall rock adjacent to the fault, material is transferred from one fault surface to the other resulting in the formation of new asperities. Ultimately, the bypass fractures cause widening of the fault core, often leaving the melted zones isolated and relatively undamaged.

influencing near-field stress orientations (Faulkner et al., 2006; Rice, 1992), altering fluid pathways via permeability enhancement or destruction (Caine, Evans, & Forster, 1996), and by changing fault strength through modifying frictional properties and fault structure (Biegel & Sammis, 2004; Mitchell & Faulkner, 2009). Wear on brittle faults is classically viewed as being an abrasive process resulting from the interaction of mechanical and geometic asperities during slip (Rabinowicz, 1965; Scholz, 2002), while fracture damage adjacent to slip zones is regarded as cumulatively forming through a range of dynamic and static processes (Blenkinsop, 2008; Mitchell & Faulkner, 2009; Wilson, Chester, & Chester, 2003; Di Toro, Nielsen, & Pennacchioni, 2005; Melosh et al., 2014). Although in recent years a number of studies have

identified new fault zone processes, including the formation of damage, the focus of much research on slip processes has entailed identifying mechanisms for dynamic weakening and understanding energy sinks for balancing earthquake energy budgets (Di Toro et al., 2011; Di Toro, Goldsby, & Tullis, 2004; Doan & Gary, 2009; Han et al., 2011; Reches & Lockner, 2010). Experimentally, the connection between high displacement slip zone processes and formation of wider low-displacement damage remains poorly explored. In this study we show a link between melt welding and the generation of both on-fault and off-fault fracture damage during successive slip events.

Repeated reactivation on unfavorably oriented faults where $\theta_r \leq 50°$ results in the development of more favorably oriented secondary fault splays at the ends of the preground fault (Figures 12d and 12e). Accommodation of slip on segments of both the preground fault and newly formed faults results in a change in sample-scale fault geometry and correspondingly to variations in normal stress and elastic strain (Figures 13a and 13b). Domains of high normal stress occur adjacent to the preground slip surface at the ends of the unfavorably oriented fault segments, favoring melt welding at the junction between the existing unfavorably oriented fault and the new fault splay (Figure 13c). Increase in cohesive strength of the welded segment on the unfavorably oriented fault results in the growth of new fractures forming a second favorably oriented segment (Figures 13c and 13d). The original secondary fault is deactivated as slip is transferred onto the new segment. Repetition of this process results in the development of a series of en echelon slip zones at the fault ends. This process leads to a progressive decrease in the length of the unfavorably oriented fault segment. It is envisaged that ultimately, with continued slip, welded fault segments on the preground fault surface could lead to the lock up of the unfavorably oriented fault and accommodation of all slip on the new, more favorably oriented faults.

4.2. Cohesive Strengthening Through Melt Welding

Fault healing, sealing, and strength recovery have traditionally been thought of as a time-dependent process resulting from compaction and cementation of the fault core, over timescales of decades to centuries (Fredrich & Evans, 1992; Tenthorey et al., 2003; Tenthorey & Cox, 2006). However, recent experimental work (current study; Proctor & Lockner, 2016; Mitchell et al., 2016) demonstrates that fault strengthening can be an almost instantaneous process, occurring after rapid episodic slip. In this study the most dramatic examples of the effects of cohesive fault strengthening occur on unfavorably oriented faults where $\theta_r \geq 55°$. At the high normal stresses associated with these ruptures, melt welding occurs over a significant area of the fault surface, almost instantaneously strengthening the fault. During subsequent reloading, a new optimally oriented fault forms in preference to reactivation of the existing fault. The evolving stress states for experiment MIS004 are considered using Mohr diagrams (Figure 14).

The first slip event occurred on the preexisting fault, where $\theta_r = 60°$. The stress state for this event is shown in the Mohr diagram by the intersection of the stress circle and the incohesive fault reactivation envelope (Figure 14a). During this rupture frictional melting occurred on the existing fault interface, welding the surfaces and increasing the cohesive strength of the fault almost instantaneously (Figure 14b). During reloading the existing misoriented fault could not be reactivated; instead, slip occurs on a new, optimally oriented fault. For this to occur, the stress conditions necessary for the failure of intact rock are achieved prior to the conditions necessary to reactivate the melt-welded existing fault (Figure 14c).

4.3. Implications for Natural Fault Zones

In this study we have used experiments to explore effects of discontinuous, grain-scale melt-welding on the behavior, and microstructural development during reactivation of laboratory faults. Our experiments have shown that melt welding on dry faults at room temperature (1) leads to near instantaneous cohesive strengthening of faults and (2) causes adhesive wear as a result of the transfer of material from one side of a fault to the other, as new shear fractures bypass previously welded zones. In nature, frictional melting can be preserved on exhumed faults where the quenched relict glass or pseudotachylyte records information of ancient seismic slip (Di Toro et al., 2005; Sibson, 1975). In this section we consider how the processes of melt welding and adhesive wear may affect the development of natural faults over a range of scales, reflecting the occurrence of a heterogeneous distribution of pseudotachylytes and melt welding on scales ranging from a few microns up to tens to hundreds of meters.

The extent of cohesive strengthening resulting from melt welding depends on the spatial distribution and volume of pseudotachylyte generated during rupture (which in turn is controlled by shear stress, slip

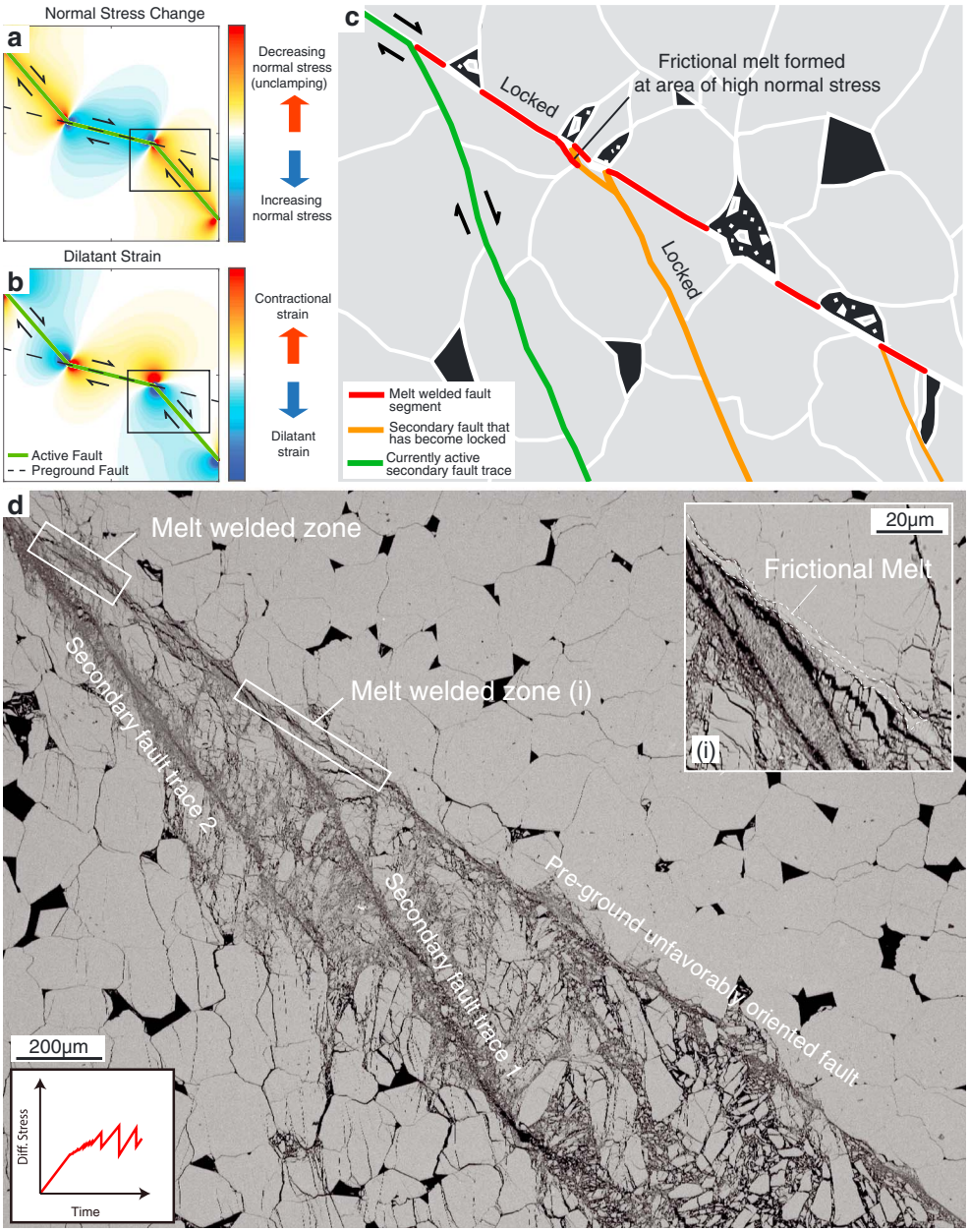

Figure 13. Effect of continued reactivation on near-fault stress fields and the resulting microstructural development. The formation of new faults segments and deactivation of others results in changes to the overall sample fault geometry. (a) Effect of changes in fault geometry on sample-scale normal stress concentrations (stress calculated using preground fault geometry) and (b) elastic strain. (c) In the region adjacent to the newly formed secondary faults, high normal stress results in an increased likelihood of frictional melting. Cohesional strengthening of the fault due to melt welding is interpreted to contribute to the lock-up and death of the first (orange) secondary fault and the formation of a new (green) secondary fault strand. (d) MIS010: An example of the microstructures produced following multiple stick-slip events in a sample where $\theta_r = 50°$. Inset shows detail of the left end of the melt-welded zone (i).

distance, slip velocity, and the composition of the host rock). On the length scales of natural faults, pseudotachylytes are discontinuous, forming patches in regions of high normal stress (Kirkpatrick & Shipton, 2009). If pseudotachylyte generation is widespread, welding can produce sufficient cohesive strengthening that faults become deactivated and slip transfers to more favorably oriented faults or other preexisting planes of weakness (e.g., joints, fractures, and cleavage planes) (Mitchell et al., 2016).

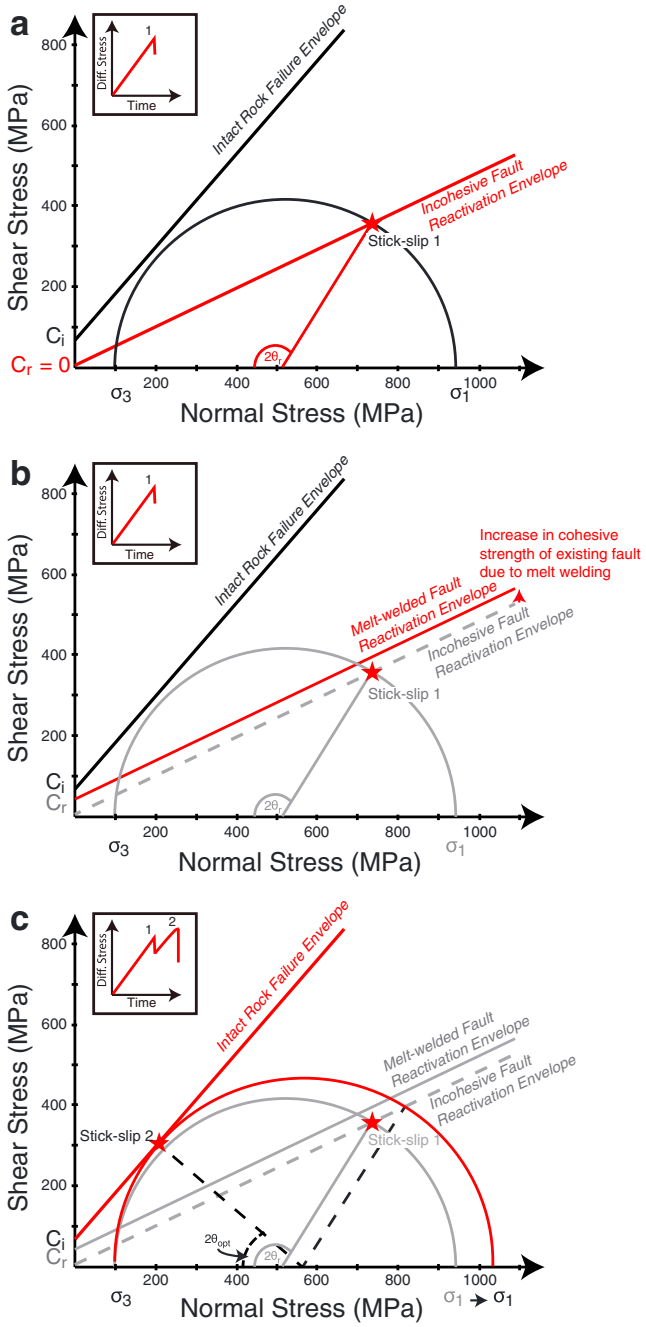

Figure 14. Melt-welding and the effect of near instantaneous cohesive strengthening of faults. Mohr diagram illustrating the experimental data from MIS004; $\theta_r = 60°$. The geometry of the failure/reactivation envelopes reflects the friction coefficient and cohesive strength defined during experimentation. C_i refers to the cohesive strength of intact rock, and C_r is an indicative estimation of the cohesive strength of the existing fault following melt welding. (a) The first stick-slip event (see inset) occurs on the preexisting fault surface as shown by the intersection of the first Mohr circle with the incohesive fault reactivation envelope. (b) During rupture shown in Figure 14a melting occurs over a considerable area of the fault interface, welding the surfaces and increasing the cohesive strength of the fault. (c) Subsequent reloading results in the Mohr circle intersecting the intact rock failure envelope prior to conditions being met that would allow the continued reactivation on the melt-welded fault.

On large faults, or if melt-welded zones on preexisting slip surfaces are sufficiently discontinuous, it may be energetically more favorable to reactivate the existing fault by (1) breaking the melt/wall rock boundary or (2) bypassing the welded zone by locally forming a new slip surface adjacent to the welded zone, rather than forming a new fault by intact rock failure. At the outcrop and macroscale Swanson (1989, 1992) identified structures coined "sidewall rip outs." Found in pseudotachylyte-bearing fault structures, they form where the fault is locally strong, potentially due to melt welding. The motion of the host rock along the planar fault surface bypasses the locked zone, ripping out a section of the opposing wall, resulting in a large-scale equivalent of adhesive wear. These structures have been recognized on natural strike-slip faults on scales ranging from 0.1 to 200 m, with similar geometric relations occurring on scales of 5–500 km (Swanson, 2005).

The formation of small-scale welded zones on experimental fault surfaces during slip of 50–500 μm and at slip velocities of 10–40 cm s^{-1} (Hayward et al., 2016) suggests that frictional melting is likely during most, if not all, dry seismic ruptures in silicate rocks at depth in the crustal seismogenic regime. However, field observations of exhumed faults suggest that pseudotachylytes are either rarely formed or rarely preserved. Of the documented examples of pseudotachylytes, many appear to be formed during single slip events (Mitchell et al., 2016; Sibson, 1975). Nonetheless, the metastable nature of pseudotachylytes indicates that in many geological settings they are unlikely to be preserved (Kirkpatrick & Rowe, 2013). Processes such as cataclastic reworking, devitrification, alteration, and dissolution can rapidly lead to overprinting and erasure of melt-welded zones, especially in areas accessible to fluids. Consequently, the role of pseudotachylytes in the evolution of fault zones is likely complex at many scales. Caution needs to be exercised when attempting to understand fault evolution from the geological record as the limited and heterogeneous preservation of structures (such as those resulting from melt welding and adhesive wear) may lead to biased or incomplete interpretation of fault zone processes.

During the months to years that pseudotachylyte feasibly retains its high cohesive strength following rupture, the presence of melt-welded zones creates heterogeneity in cohesive strength on the fault surface. Importantly, it is the cohesive strength of the pseudotachylyte that plays a significant role in the development of adhesive wear processes by creating local stress concentrations around the ends of welded zones, enhancing the formation of microfractures. On the grain scale, dynamic welding of asperity contacts has previously been identified as one mechanism for adhesive wear in metals and is considered instrumental in the early stages surface damage (Bowden & Tabor, 1950). We suggest that on timescales of rupture recurrence, the distribution of thin layers of pseudotachylyte may also play a significant role as frictional asperities and thereby influence the development of the fault core and distribution of lateral fracture damage during the early stages of fault development.

5. Conclusions

Varying the orientation of preexisting fault surfaces has allowed experimental examination of the influence of normal stress and far-field

stress orientations on the reactivation of faults, generation of frictional melt, and development of off-fault fracture damage zones. With increasing reactivation angle, the normal stress acting on the fault increases and the dynamic behavior evolves from dominantly stable sliding, through small stick slip to large displacement episodic slip events. This change in behavior is associated, first, with an increase in the volume and distribution of frictional melt that is produced and, second, by increasing levels of fracture damage around the fault.

The distribution of melt-welded domains plays a critical role in localizing the distribution and style of off-fault fracture damage during successive slip events. Damage is thought to occur both quasi-statically and dynamically. Welded sections locally lock the fault, perturbing the surrounding stress states. Fractures form preferentially in dilatant regions, bypassing the melt-welded zones through the formation of either (1) more favorably oriented secondary faults strands at the fault ends or (2) sidewall rip-outs/bypass faults that form parallel to the preground fault surface. Transfer of melt-adhered material from one side of the fault to the other changes fault topography, forming geometric asperities on the interface. Progressive cataclastic deformation of asperities during successive slip events contributes to the formation of gouge. Where faults are repeatedly reactivated, melt welding leads to widening of the fault core with successive slip events.

During episodic rapid slip on unfavorably oriented faults ($\theta_r \geq 55°$) melt welding is especially significant, with up to ~50% of the fault interface becoming welded. This process results in a near-instantaneous increase in fault cohesive strength. Widespread melt welding is sufficient to cause fault lock-up and formation of a new, optimally oriented fault during subsequent re-loading.

Our experiments demonstrate that pseudotachylyte is strong under brittle conditions. Melt welding can lead to frictional lock-up and fault death. However, where the heterogeneous distribution of melt welding on fault surfaces does not lead to lock-up, the distribution of pseudotachylyte layers can play a role in the development of low displacement, off-fault fracture damage, and the formation of high displacement wear damage in fault cores.

Acknowledgments

A. Schubnel generously supplied the Fontainebleau sandstone used in this study. H. Miller and H. Kokkonen are thanked for their technical support. The electron microscopy work was undertaken at the Australian National University Centre for Advanced Microscopy. The National Laboratory of X-Ray Micro Computed Tomography at the ANU College Science is thanked for assistance with the X-Ray tomography. The authors thank R. Sibson for stimulating discussion on frictional melting and fault reactivation. B. Proctor and J. Spray are thanked for their very helpful and careful reviews, which contributed greatly to clarity of this manuscript. This study was supported by Australian Research Council grant DP130102687 and an Australian National University Major Equipment Grant (16MEC12). K. Hayward gratefully acknowledges scholarship support from the Australian Government Research Training Program.

References

Biegel, R. L., & Sammis, C. (2004). Relating fault mechanics to fault zone structure. *Advances in Geophysics*, *47*, 65–111. https://doi.org/10.1016/S0065-2687(04)47002-2

Blenkinsop, T. G. (2008). Relationships between faults, extension fractures and veins, and stress. *Journal of Structural Geology*, *30*(5), 622–632. https://doi.org/10.1016/j.jsg.2008.01.008

Bowden, F. P., & Tabor, D. (1942). Mechanism of metallic friction. *Nature*, *150*(3798), 197–199. https://doi.org/10.1038/150197a0

Bowden, F. P., & Tabor, D. (1950). *Friction and Lubrication of Solids* (Vol. 1). Oxford: Clarendon.

Brantut, N., & Platt, J. (2016). Dynamic weakening and the depth dependence of earthquake faulting. In M. Y. Thomas, T. M. Mitchell, & H. S. Bhat (Eds.), *Fault Zone Dynamic Processes: Evolution of Fault Properties During Seismic Rupture* (pp. 171–194). Hoboken, NJ: John Wiley.

Byerlee, J. D. (1978). Friction of rocks. *Pure and Applied Geophysics*, *116*(4-5), 615–626. https://doi.org/10.1007/BF00876528

Caine, J. S., Evans, J. P., & Forster, C. B. (1996). Fault zone architecture and permeability structure. *Geology*, *24*(11), 1025–1028. https://doi.org/10.1130/0091-7613(1996)024%3C1025:FZAAPS%3E2.3.CO;2

Chester, F. M., & Chester, J. S. (2000). Stress and deformation along wavy frictional faults. *Journal of Geophysical Research*, *105*(B10), 23,421–23,430. https://doi.org/10.1029/2000JB900241

Childs, T. H. C. (1980). The sliding wear mechanisms of metals, mainly steels. *Tribology International*, *13*(6), 285–293. https://doi.org/10.1016/0301-679X(80)90092-4

Collettini, C., & Holdsworth, R. E. (2004). Fault zone weakening and character of slip along low-angle normal faults: Insights from the Zuccale fault, Elba, Italy. *Journal of the Geological Society*, *161*, 1039–1051. https://doi.org/10.1144.0016-764903-179.

Collettini, C., Niemeijer, A., Viti, C., & Marone, C. (2009). Fault zone fabric and fault weakness. *Nature*, *462*, 907–910. https://doi.org/10.1038/nature08585.

Cox, S. F. (1998). Slickenlines produced experimentally at hydrothermal conditions. In A. W. Snoke, J. Tullis, & V. R. Todd (Eds.), *Fault-Related Rocks: A Photographic Atlas* (pp. 136–137). NJ: Princeton University Press.

Cox, S. F. (2010). The application of failure mode diagrams for exploring the roles of fluid pressure and stress states in controlling styles of fracture-controlled permeability enhancement in faults and shear zones. *Geofluids*, *10*, 217–233.

David, E. C., Fortin, J., Schubnel, A., & Guéguen, Y. (2013). Laboratory measurements of low and high-frequency elastic moduli in Fontainebleau sandstone. *Geophysics*, *78*(5), 369–379.

Di Toro, G., & Pennacchioni, G. (2005). Fault plane processes and mesoscopic structure of a strong-type seismogenic fault in tonalites (Adamello batholith, Southern Alps). *Tectonophysics*, *402*, 55–80. https://doi.org/10.1016/j.tecto.2004.12.036

Di Toro, G., Goldsby, D. L., & Tullis, T. E. (2004). Friction falls towards zero in quartz rock as slip velocity approaches seismic rates. *Nature*, *427*, 436–439. https://doi.org/10.1038/nature02249

Di Toro, G., Nielsen, S., & Pennacchioni, G. (2005). Earthquake ruputre dynamics frozen in exhumed ancient faults. *Nature*, *436*, 1009–1012. https://doi.org/10.1038/nature03910

Di Toro, G., Han, R., Hirose, T., De Paola, N., Nielsen, S., Mizoguchi, K., … Shimamoto, T. (2011). Fault lubrication during earthquakes. *Nature*, *471*, 494–498. https://doi.org/10.1038/nature09838

Dieterich, J. H. (1979). Modelling of rock friction: 1. Experimental results and constitutive equations. *Journal of Geophysical Research*, *84*(B5), 2161–2168. https://doi.org/10.1029/JB084iB05p02161

Doan, M., & Gary, G. (2009). Rock pulverization at high strain rate near the San Andreas fault. *Nature Geoscience*, *2*, 709–712. https://doi.org/10.1038/ngeo640

Faulkner, D. R., Mitchell, T. M., Healy, D., & Heap, M. J. (2006). Slip on 'weak' faults by the rotation of regional stress in the fracture damage zone. *Nature*, *444*, 922–925. https://doi.org/10.1038/nature05353

Fournier, R. O. (1996). Compressive and tensile failure at high fluid pressure where preexisting fractures have cohesive strength, with application to the San Andreas Fault. *Journal of Geophysical Research*, *101*, 499–509.

Fredrich, J. T., & Evans, B. (1992). Strength recovery along simulated faults by solution transfer processes. In *The 33th US Symposium on Rock Mechanics*. New Mexico: American Rock Mechanics Association Santa Fe.

Griffith, W. A., Nielsen, S., Di Toro, G., & Smith, S. A. F. (2010). Rough faults, distributed weakening and off fault deformation. *Journal of Geophysical Research*, *115*, B08409. https://doi.org/10.1029/2009JB006925

Han, R., Hirose, T., Shimamoto, T., Lee, Y., & Ando, J. (2011). Granular nanoparticles lubricate faults during seismic slip. *Geology*, *39*, 599–602. https://doi.org/10.1130/G31842.1

Hayward, K. S., Cox, S. F., Fitz Gerald, J. D., Slagmolen, B. J. J., Shaddock, D. A., Forsyth, P. W. F., … Hawkins, R. P. (2016). Mechanical amorphization, flash heating, and frictional melting: Dramatic changes to fault surfaces during the first millisecond of earthquake slip. *Geology*, *44*(12), 1043–1046. https://doi.org/10.11/G38242.1

Hoek, E. (1965). Rock fracture under static stress conditions. National Mechanical Engineering Research Institute, *Council for Scientific and Industrial Research CSIR special report: MEG 383*, 1–235.

Holdsworth, R. E. (2004). Weak faults—Rotten cores. *Science*, *303*(5655), 181–182. https://doi.org/10.1126/science.1092491

Jaeger, J. C., Cook, N. G., & Zimmerman, R. W. (2007). *Fundamentals of Rock Mechanics* (4th ed.). Malden: Blackwell.

Karner, S. L., Marone, C., & Evans, B. (1997). Laboratory study of fault healing and lithification in simulated fault gouge under hydrothermal conditions. *Tectonophysics*, *277*(1-3), 41–55. https://doi.org/10.1016/S0040-1951(97)00077-2

Kerridge, M. (1955). Metal transfer and the wear process. *Proceedings of the Physical Society. Section B*, *68*(7), 400–407. https://doi.org/10.1088/0370-1301/68/7/302

Kirkpatrick, J. D., & Rowe, C. D. (2013). Disappearing ink: How pseudotachylytes are lost from the rock record. *Journal of Structural Geology*, *53*, 183–198.

Kirkpatrick, J. D., & Shipton, Z. K. (2009). Geologic evidence for multiple slip weakening mechanisms during seismic slip in crystalline rock. *Journal of Geophysical Research*, *114*, B12401. https://doi.org/10.1029/2008JB006037

Limaye, A. (2012). Dristhi: A volume exploration and presentation tool. *Proceedings: Developments in X Ray tomography*, *VIII*, 8506.

Lockner, D. A., Byerlee, J. D., Kuksenko, V., Ponomarev, A., & Sidorin, A. (1991). Quasi-static fault growth and shear fracture energy in granite. *Nature*, *350*(6313), 39–42. https://doi.org/10.1038/350039a0

Logan, J. M., Dengo, C. A., Higgs, N. G., & Wang, Z. Z. (1992). Fabrics of experimental fault zones: Their development and relationship to mechanical behavior. In B. Evans & T.-F. Wong (Eds.), *Fault Mechanics and Transport Properties of Rocks*, (pp. 33–67). London: Academic Press, Ltd.

Melosh, B. L., Rowe, C. D., Smit, L., Groenewald, C., Lambert, C. W., & Macey, P. (2014). Snap Crackle Pop: Dilational fault breccias record seismic slip below the brittle-plastic transition. *Earth and Planetary Science Letters*, *403*, 432–445. https://doi.org/10.1016/j.epsl.2014.07.002

Mitchell, T. M., & Faulkner, D. R. (2009). The nature and origin of off-fault damage surrounding strike-slip fault xones with a wide range of displacements: A field study from the Atacama fault zone, northern Chile. *Journal of Structural Geology*, *31*, 802–816. https://doi.org/10.1016/j.jsg.2009.05.002

Mitchell, T. M., Toy, V., Di Toro, G., Renner, J., & Sibson, R. H. (2016). Fault welding by pseudotachylyte formation. *Geology*, *44*(12), 1059–1062. https://doi.org/10.1130/G38373.1

Mount, V. S., & Suppe, J. (1987). State of stress near the San Andreas fault: Implications for wrench tectonics. *Geology*, *15*(12), 1143–1146. https://doi.org/10.1130/0091-7613(1987)15%3C1143:SOSNTS%3E2.0.CO;2

O'Hara, K. (1992). Major and trace element constraints on the petrogenesis of fault-related pseudotachylyte, western Blue Ridge province, North Carolina. *Tectonophysics*, *204*(3-4), 279–288. https://doi.org/10.1016/0040-1951(92)90312-T

Passchier, C. W., & Trouw, R. A. (2005). *Microtectonics* (2nd ed.). Berlin: Springer.

Passelègue, F. X., Latour, S., Schubnel, A., Neilsen, S., Bhat, H. S., & Madariaga, R. (2016). Influence of fault strength on precursory processes during laboratory earthquakes. In M. Thomas, T. M. Mitchell, & H. S. Bhat (Eds.), *Fault Zone Dynamic Processes: Evolution of Fault Properties During Seismic Rupture*, *Geophysical Monograph 227*, (pp. 229–242). Washington, DC: American Geophysical Union.

Paterson, M. S. (1970). A high-pressure, high-temperature apparatus for rock deformation. *International Journal of Rock Mechanics and Mining Science and Geomechanics Abstracts*, *7*(5), 517IN3525-524IN4526.

Paterson, M. S., & Wong, T. F. (2005). *Experimental Rock Deformation—The Brittle Field* (2nd ed.). Berlin: Springer.

Pimienta, L., Fortin, J., & Guéguen, Y. (2016). Effect of fluids and frequencies on Poisson's ratio of sandstone samples. *Geophysics*, *81*(2), 35–47.

Proctor, B., & Lockner, D. A. (2016). Pseudotachylyte increases the post-slip strength of faults. *Geology*, *44*(12), 1003–1006. https://doi.org/10.1130/G38349.1

Rabinowicz, E. (1965). *Friction and Wear in Materials*. New York: John Wiley.

Reches, Z., & Dewers, T. A. (2005). Gouge formation by dynamic pulverization during earthquake rupture. *Earth and Planetary Science Letters*, *235*, 361–374. https://doi.org/10.1016/j.epsl.2005.04.009

Reches, Z., & Lockner, D. A. (2010). Fault weakening and earthquake instability by powder lubrication. *Nature*, *467*, 452–455. https://doi.org/10.1038/nature09348

Rice, J. R. (1992). Pore pressure distribution and the weakness of the San Andreas Fault. In B. Evans & T.-F. Wong (Eds.), *Fault Mechanics and Transport Properties of Rocks*. (pp. 475–503) London: Academic Press Limited.

Rice, J. R. (2006). Heating and weakening of faults during earthquake slip. *Journal of Geophysical Research*, *111*, B05311. https://doi.org/10.1029/2005JB004006

Rutter, E., & Hackston, A. (2017). On the effective stress law for rock-on-rock frictional sliding, and fault slip triggered by means of fluid injection. *Philosophical Transactions of the Royal Society A*, *375*, 1–20.

Sakellariou, A., Sawkins, T., Senden, T., & Limaye, A. (2004). X-ray tomography for mesoscale physics applications. *Physica A: Statistical Mechanics and its Applications*, *339*, 152–158. https://doi.org/10.1016/j.physa.2004.03.055

Scholz, C. H. (2002). *The Mechanics of Earthquakes and Faulting* (2nd ed.). New York: Cambridge University Press. https://doi.org/10.1017/CBO9780511818516

Sibson, R. H. (1975). Generation of pseudotachylyte by ancient seismic faulting. *Geophysical Journal International*, *43*(3), 775–794. https://doi.org/10.1111/j.1365-246X.1975.tb06195.x

Sibson, R. H. (1985). A note on fault reactivation. *Journal of Structural Geology*, *7*(6), 751–754. https://doi.org/10.1016/0191-8141(85)90150-6

Sibson, R. H. (1989). Earthquake faulting as a structural process. *Journal of Structural Geology*, *11*(1-2), 1–14. https://doi.org/10.1016/0191-8141(89)90032-1

Sibson, R. H. (1990). Rupture nucleation on unfavourably oriented faults. *Bulletin of the Seismological Society of America*, *80*, 1580–1604.

Sibson, R. H. (2007). An episode of fault-valve behaviour during compressional inversion?—The 2004 M_J6.8 Mid-Niigata Prefecture, Japan, earthquake sequence. *Earth and Planetary Science Letters*, *257*, 188–199. https://doi.org/10.1016/j.epsl.2007.02.031

Sibson, R. H. (2012). Reverse fault rupturing: Competition between non-optimal and optimal fault orientations. *Geological Society, London, Special Publications*, *367*, 39–50. https://doi.org/10.1144/SP367.4

Sibson, R. H., Robert, F., & Poulsen, K. H. (1988). High-angle reverse faults, fluid pressure cycling and mesothermal gold-quartz deposits. *Geology*, *16*(6), 551–555. https://doi.org/10.1130/0091-7613(1988)016%3C0551:HARFFP%3E2.3.CO;2

Spray, J. G. (1992). A physical basis for the frictional melting of some rock-forming minerals. *Tectonophysics*, *204*, 223–242.

Spray, J. G. (1995). Pseudotachylyte controversy: Fact or friction. *Geology*, *23*(12), 1119–1122. https://doi.org/10.1130/0091-7613(1995)023%3C1119:PCFOF%3E2.3.CO;2

Streit, J. E., & Cox, S. F. (2001). Fluid pressures at hypocenters of moderate to large earthquakes. *Journal of Geophysical Research*, *106*(2), 2235–2243.

Swanson, M. T. (1989). Sidewall ripouts in strike-slip faults. *Journal of Structural Geology*, *11*(8), 933–948. https://doi.org/10.1016/0191-8141(89)90045-X

Swanson, M. T. (1992). Fault structure, wear mechanisms and rupture processes in pseudotachylyte generation. *Tectonophysics*, *204*(3-4), 223–242. https://doi.org/10.1016/0040-1951(92)90309-T

Swanson, M. T. (2005). Geometry and kinematics of adhesive wear in brittle strike-slip fault zones. *Journal of Structural Geology*, *27*, 871–887. https://doi.org/10.1016/j.jsg.2004.11.009

Tenthorey, E., & Cox, S. F. (2006). Cohesive strengthening of fault zones during the interseismic period: An experimental study. *Journal of Geophysical Research*, *111*, B09202. https://doi.org/10.1029/2005JB004122

Tenthorey, E., Cox, S. F., & Todd, H. F. (2003). Evolution of strength recovery and permeability during fluid-rock reaction in experimental fault zones. *Earth and Planetary Science Letters*, *206*(1-2), 161–172. https://doi.org/10.1016/S0012-821X(02)01082-8

Toda, S., Stein, R. S., Sevilgen, V., & Lin, J. (2011). Coulomb 3.3 graphic-rich deformation and stress-change software for earthquake, tectonic, and volcano research and teaching—User guide. U.S. Geological Survey Open-File Report 2011–1060, 1–63.

Varslot, T., Kingston, A., Myers, G., & Sheppard, A. (2011). High-resolution helical cone-beam micro-CT with theoretically-exact reconstruction from experimental data. *Medical Physics*, *38*, 5459–5476. https://doi.org/10.1118/1.3633900

Wernicke, B. (1995). Low-angle normal faults and seismicity: A review. *Journal of Geophysical Research*, *100*(B10), 20,159–20,174. https://doi.org/10.1029/95JB01911

Wilson, J. E., Chester, J. S., & Chester, F. M. (2003). Microfracture analysis of fault growth and wear processes, Punchbowl Fault, San Andreas System, California. *Journal of Structural Geology*, *25*(11), 1855–1873. https://doi.org/10.1016/S0191-8141(03)00036-1